

Implementation of a Dynamic Equation Constraint based on the Steady State Momentum Equations within the WRF Hybrid Ensemble-3DVar Data Assimilation System and Test with Radar T-TREC Wind Assimilation for Tropical Cyclone Chanthu (2010)

Xin Li^{1,2}, Jie Ming¹, Ming Xue^{1,3}, Yuan Wang¹, Kun Zhao¹

¹Key Laboratory of Mesoscale Severe Weather/MOE and School of Atmospheric Sciences, Nanjing University, Nanjing 210023, China

²Jiangsu Research Institute of Meteorological Sciences, Nanjing 210009, China

³Center for Analysis and Prediction of Storms, and School of Meteorology, University of Oklahoma, Norman, Oklahoma, USA, 73072

October, 2014

Submitted to Journal of Geophysical Research

Revised February, 2015

Corresponding author address:

Dr. Jie Ming
Key Laboratory of Mesoscale Severe Weather/MOE and School of Atmospheric Sciences,
Nanjing University, Nanjing 210023, China
jming@nju.edu.cn

Abstract

Proper dynamic equation constraints in data assimilation (DA) systems can help improve balance of analyzed atmospheric state. The formulation of ensemble-variational DA algorithms allows for easy incorporation of such constraints but their impacts within such DA systems have been little studied. A dynamic constraint based on the steady momentum equations is incorporated into the WRF (Weather Research and Forecasting) hybrid ensemble-3DVar (En3DVar) DA system as a weak constraint. The constraint aims at improving the coupling and balance among wind and thermodynamic state variables, especially when few state variables are directly observed. The scheme is applied to the assimilation of radar T-TREC (Typhoon-Tracking Radar Echo by Correlation) winds at a convection-allowing resolution, for landfalling typhoon, Chanthu (2010), when it was within the range of a coastal radar.

Parallel experiments using the 3DVar and En3DVar with and without the dynamic constraint are run to examine the impact of the constraint. The flow-dependent ensemble covariance used in En3DVar helps to update unobserved pressure and temperature fields in a dynamically more consistent way compared to the static covariance; the added dynamic constraint produces more accurate pressure within the typhoon. The pressure field improved by the dynamic constraint also leads to better temperature and moisture analyses within the variational minimization through flow-dependent cross-covariance. En3DVar analysis with the dynamic constraint produces the best intensity forecast for the typhoon, in terms of the minimum sea level pressure and maximum surface wind speed. Additional sensitivity experiments examine the impact of the weight of the dynamic constraint.

1. Introduction

Tropical cyclones (TCs) are among the most disastrous natural hazards for coastal countries. Accurate prediction of TC track and intensity is crucial for the protection of lives and properties. In addition to accurate prediction models, accurate initial conditions are also a very important factor for the prediction of TCs, which requires well-performed data assimilation (DA) systems.

Many efforts have been made to improve the TC initial condition through DA. Within a three-dimensional variational (3DVar) (Sasaki 1970a, b; Talagrand and Courtier 1987; Parrish and Derber 1992) framework, Xiao et al. (2000) developed a so-called bogus data assimilation (BDA) based on the use of synthetic vortex with presumed estimated parameters of TC size and intensity. Efforts have also been made to directly assimilate using 3DVar methods TC inner-core observations such as those from Doppler weather radar (e.g., Xiao et al. 2005; Zhao and Xue 2009; Pu et al. 2009), in order to initialize the three-dimensional TC structures. The 3DVar method is widely used and computationally efficient but its typically used climatological static background error covariance usually has no specific knowledge about the presence of TC.

An alternative to the variational (VAR) method is the ensemble-based DA method. Evensen (1994) firstly proposed the ensemble Kalman filter (EnKF) for an oceanographic application; since then EnKF has been applied to numerous atmospheric problems. The performance of EnKF has been demonstrated for TC DA and prediction in a number of studies (e.g., Chen and Snyder 2007; Zhang et al. 2009; Schwartz et al. 2012; Liu et al. 2012; Weng and Zhang 2012; Dong and Xue 2013). Zhang et al. (2009) demonstrated the better performance of EnKF over 3DVar in track and intensity forecasts of hurricane Humberto (2007) when assimilating coastal radar data; the EnKF case benefited from the flow-dependent background error covariance derived from the ensemble.

Although the ensemble-derived flow-dependent covariance is superior to the static one used in VAR method, it does contain significant sampling error due to the typically rather small ensemble sizes which are limited by the high computational costs.

A hybrid ensemble-variational scheme has been proposed (Hamill and Snyder 2000; Lorenc 2003; Buehner 2005) to help alleviate the sampling error problem. A hybrid method combines the ensemble and static covariances within a VAR framework. A hybrid scheme can be especially beneficial when ensemble size is small and/or when model error is large (Wang et al. 2008b). Furthermore, the variational framework provides a straightforward way for implementing dynamic constraints.

Lorenc (2003) proposed a so-called extended control variable method for easily incorporating ensemble covariances in a VAR framework. Wang et al. (2008a,b) describe the implementation of this method within the WRF-3DVar framework, to established a WRF (Skamarock et al. 2008) hybrid ensemble-3DVar (En3DVar) DA system. With this WRF En3DVar system, Wang (2011) explored the impact of flow-dependent ensemble covariance on the assimilation of conventional observations for hurricanes compared to static covariance in standard 3DVar. The locations of TCs are systematically adjusted during the assimilation using flow-dependent covariance and improved track forecasts are also obtained. Schwartz et al. (2013) also compared the performance of the WRF En3DVar hybrid system coupled with an ensemble adjustment Kalman filter (EAKF, Anderson 2001) with that of WRF 3DVar for TC initializations, and found better predictions of TC tracks when using the hybrid; mean track errors for 72 hour forecasts launched every 6 hours from continuously cycled analyses over a 3.5 week period were examined. Wang (2011) examined two individual hurricane cases and the WRF En3DVar was coupled with the ensemble transform Kalman filter (ETKF, Bishop et al. 2001). Wang (2011) and Schwartz et al. (2013) used 30 and 45 km grid spacings, respectively, and both focused on track forecasting. Li et al. (2012) examined the impacts of assimilating radar radial velocity (V_r) data on a landfalling hurricane using the WRF En3DVar hybrid and 3DVar at a 5 km grid spacing, and found that the hybrid scheme improved the analysis of the inner-core structures of the hurricane as well the forecasting of the hurricane track and intensity. Despite these encouraging results, applications of the hybrid method to TC assimilation and prediction remain very limited.

For landfalling TCs, data from coastal Doppler radars have been demonstrated effective for the initialization of TC inner-core structures and for improving the resulting forecasts (e.g., Zhao and Xue 2009; Pu et al. 2009; Zhao et al. 2012a, b). However, studies have also shown challenges in analyzing the pressure field consistently when only radar wind is assimilated. Wang et al. (2014) discussed this issue and showed that most of the pressure adjustment towards gradient balance was achieved through model adjustment during the forecast step, and it takes a number of assimilation cycles to establish such balance. Dong and Xue (2013) also noted this problem when assimilating coastal radar data using EnKF for a hurricane, and Xue and Dong (2013) improved the pressure analysis by assimilating best-track minimum sea level pressure (MSLP) data.

A hybrid ensemble-variational framework provides an opportunity for combining flow-dependent covariance and equation constraints. Equations that can help enforce quasi-gradient balance for analyzed TCs can potentially improve the analysis of pressure fields when assimilating radar winds. In this study, we explore the use of such equation constraints. The steady state horizontal momentum equations are introduced into the WRF En3DVar cost function as a weak constraint (Sasaki 1970c; Gao et al. 1999; Liang et al. 2007; Ge et al. 2012), with its relative importance in the cost function determined by the weight of the constraint term.

In Li et al. (2013) and Wang et al. (2014), the assimilation of the T-TREC (Typhoon - Tracking

Radar Echo by Correlation) winds retrieved from radar reflectivity and radial velocity data (Wang et al. 2011), using 3DVar and EnKF respectively, was shown to perform better than the direct assimilation of V_r for TC analysis and forecast, due to the larger spatial coverage of reflectivity data and the more complete TC circulations thus derived. Based on these advantages, this study also assimilates the T-TREC-retrieved winds and explores for the first time their assimilation with a hybrid En3DVar method. The T-TREC technique (Wang et al. 2011) extends the traditional TREC (Tracking Radar Echo by Correlation) method (Tuttle and Gall 1999; Harasti et al. 2004) and retrieves horizontal circulations within TCs from radar reflectivity data, with supplementary use of V_r information.

The hybrid WRF En3DVar with the dynamic constraints is applied to the assimilation of radar T-TREC winds for typhoon Chanthu (2010) which made landfall in Guangdong Province of China. As a pilot study, and to focus on the impacts of introducing the dynamic equation constraints with and without flow-dependent ensemble covariance, a single time analysis is performed to initialize typhoon Chanthu in this study. The results from 3DVar/En3DVar (En3DVar with pure static covariance is effectively 3DVar) with dynamic constraint are compared to those from traditional 3DVar/En3DVar without the constraint.

The rest of this paper is organized as follows. Section 2 describes the theory of hybrid En3DVar scheme with dynamic constraint. The overview of T-TREC wind data for typhoon Chanthu (2010), the description of forecasting model, and experimental configurations are explained in Section 3. Section 4 examines the results of initialization and deterministic forecasting for Chanthu (2010). Sensitivity experiments considering the choice of dynamic weight in the cost function are discussed in Section 5. Summary and conclusions are presented in Section 6.

2. Methodology

a. WRF hybrid En3DVAR system

In this section, we first briefly describe the framework of current WRF hybrid En3DVar system (Wang et al. 2008a, b). The analysis field is obtained via minimizing the cost function as

$$\begin{aligned}
 J &= J_o + \beta_1 J_b + \beta_2 J_e \\
 &= \frac{1}{2} (\mathbf{d} - \mathbf{H}\mathbf{x}')^T \mathbf{O}^{-1} (\mathbf{d} - \mathbf{H}\mathbf{x}') + \beta_1 \frac{1}{2} (\mathbf{x}_1')^T \mathbf{B}^{-1} (\mathbf{x}_1') + \beta_2 \frac{1}{2} (\mathbf{a})^T \mathbf{A}^{-1} (\mathbf{a})
 \end{aligned} \tag{1}$$

The first two terms on the right hand side (RHS) of Eq. (1) are the traditional 3DVar terms. J_o is the observation term, \mathbf{O}^{-1} is the observation error covariance matrix; the innovation vector \mathbf{d} is defined as $\mathbf{d} = \mathbf{y}_o - H(\mathbf{x}_b)$, where \mathbf{y}_o is the observation vector, \mathbf{x}_b the background state vector, H the nonlinear observation operator. \mathbf{H} is the linearization of H . J_b is the background term associated with static background covariance \mathbf{B} derived using the NMC (National Meteorological Center) method (Derber and Parrish 1992); \mathbf{x}_1' stands for the analysis increment. The ‘cv5’ option of static covariance \mathbf{B} used in this study includes the control variables of stream function ψ , unbalanced velocity potential χ_u , unbalanced temperature T_u , unbalanced surface pressure P_{su} , and “pseudo” relative humidity rh . The third term on the RHS of J_e represents the background term associated with ensemble covariance. The terms with static covariance and ensemble covariance can be weighted by the tunable parameter β_1 and β_2 during the

minimization process. For the conservation of the total background error covariance, $\frac{1}{\beta_1} + \frac{1}{\beta_2} = 1$.

When $\frac{1}{\beta_1} = 1$, the analysis reverts back to the traditional 3DVar; when $\frac{1}{\beta_2} = 1$, full weight is assigned to the flow-dependent covariance. The ensemble covariance is incorporated into the VAR framework through an extended control variable \mathbf{a} . The full analysis increment \mathbf{x}' is the sum of traditional 3DVar increment \mathbf{x}'_1 and the increment associated with the ensemble covariance,

$$\mathbf{x}' = \mathbf{x}'_1 + \sum_{k=1}^K \mathbf{a}_k \circ \mathbf{x}_k^e \quad (2)$$

Here, \mathbf{a}_k denotes the extended control variable (Lorenz, 2003) and \mathbf{x}_k^e is the ensemble perturbation state vector for each ensemble member. The symbol \circ denotes the Schur product (element by element product).

As described in Wang et al. (2008a), \mathbf{A} in J_e is the ensemble covariance localization matrix. Both horizontal and vertical localizations are applied in this study. The horizontal localization is modeled by the recursive filter transform. For vertical localization, the physical distance-dependent vertical correlation is used based on the Empirical orthogonal functions (EOFs), following Li et al. (2012).

b. The hybrid En3DVar scheme with dynamic constraint

Based on the existing WRF hybrid En3DVar system, a weak penalty constraint term J_c is added into the cost function in this study. The total cost function therefore is defined as

$$J = J_o + \beta_1 J_b + \beta_2 J_e + J_c \quad (3)$$

The fourth term on the RHS of Eq. (3) includes the dynamic constraint defined as following:

$$J_c = \frac{1}{2} G(\mathbf{x})^T \Gamma^{-1} G(\mathbf{x}) \quad (4)$$

Where $G(\mathbf{x})$ represents the imposed dynamic equation and Γ^{-1} is the dynamic weight. For the purpose of TC assimilation, the momentum equations with steady assumption are used which constrain the mass field and the momentum field. The nonlinear operator G which represents the dynamic equation of WRF sigma coordinate is given by

$$G = \bar{V} \cdot \nabla_{\sigma} \bar{V} + f \cdot \bar{k} \times \bar{V} + \nabla_{\sigma} \phi + \frac{1}{\rho} \nabla_{\sigma} p \quad (5)$$

Where \bar{V} is the vector of horizontal velocity (wind components u and v), f the Coriolis coefficient, ϕ the geopotential height, ρ the density, and p the pressure.

Through the minimizing iteration, the gradient item of J_c with respect to is

$$\nabla J_c = \mathbf{G}^T \Gamma^{-1} [\mathbf{G}\mathbf{x}' + G(\mathbf{x}_b)] \quad (6)$$

where dynamic weight matrix Γ^{-1} is a diagonal matrix with the same value for the diagonal elements. After linearizing Eq. (5), the tangent linear operator \mathbf{G} is

$$\mathbf{G} = \bar{V} \cdot \nabla_{\sigma} \bar{V}' + \bar{V}' \cdot \nabla_{\sigma} \bar{V} + f \cdot \bar{k} \times \bar{V}' + \nabla_{\sigma} \phi' + \frac{1}{\rho} \nabla_{\sigma} p' \quad (7)$$

there the overbar denotes the background state while the prime denotes the increment.

During each iteration step, the geopotential height and pressure increments, ϕ' and p' , need to be diagnosed for the dynamic constraint, apart from the increments of five direct analyzed variables horizontal (wind u and v , temperature t , mixing ratio q and surface pressure ps). The pressure increment p' is related to the increment of dry surface pressure μ_d' and the increment of mixing ratio q' (Skamarock et al. 2008).

$$dp' = \mu_d' (1 + \bar{q}) d\eta + q' \bar{\mu}_d d\eta \quad (8)$$

The three-dimensional pressure increment p' is obtained by vertically integrating the linear Eq.(8) from the top level to the bottom level. μ_d' is calculated by removing the moisture contribution from the increment of surface pressure p_s' as follows

$$\mu_d' = \frac{p_s' - \bar{\mu}_d \int_0^1 q' d\eta}{\int_0^1 (1 + \bar{q}) d\eta} \quad (9)$$

For the increment of geopotential height ϕ' , hydrostatic relation is used with the dry surface pressure μ_d' and the increment of dry inverse density α_d' (Skamarock et al. 2008),

$$d\phi' = (-\bar{\mu}_d \alpha_d' - \bar{\alpha}_d \mu_d') d\eta \quad (10)$$

The three-dimensional increment of geopotential height ϕ' can be obtained by vertically integrating Eq.(10) from the bottom level up to the top level.

The linear operator \mathbf{G} is discretized, and its adjoint code \mathbf{G}^T is developed accordingly within the existing WRF hybrid En3DVar system. The correctness of the gradient of cost function (Eq.(6)) after adding the constraint item should be verified to make sure minimization works successfully. Similar to the previous studies (e.g., Courtier et al. 1987; Sun et al. 1991; Gao et al. 2012; Wang et al. 2013), we expand the cost function $J(x)$ at the direction $\nabla_x J$ using the Taylor series, let

$$\Phi(\alpha) \equiv \frac{J(x + \alpha \nabla_x J) - J(x)}{\alpha \nabla_x J \cdot \nabla_x J} = 1.0 + O(\alpha \|\nabla_x J\|) \quad (11)$$

For the values of α which are small but not too close to zero, $\Phi(\alpha)$ should be close to 1 if the gradient is computed correctly. The updated hybrid En3DVar system with dynamic constraint has been checked using this method. The value of $\Phi(\alpha)$ is shown in Fig. 1a when α takes the values from 10^{-3} to 10^{-16} . Between 10^{-5} and 10^{-15} , the value of 1 is obtained for $\Phi(\alpha)$ suggesting that the gradient calculation is correct. Besides, Fig. 1b shows the degree of approximation based on how $\Phi(\alpha)$ is close to 1.

To further verify that the minimization process works well after including the dynamic constraint, the total cost function and the observation and constraint terms as well as their gradient norms are examined in Fig. 2 with 1 outer loop and 100 inner loop minimization iterations, similar to that in Gao et al. (2001). It is verified that the total cost function and the two individual terms all decrease steadily in the minimization process (Fig. 2a), as do their corresponding gradient norms in general (Fig. 2b).

3. Experimental design

a. T-TREC-retrieved wind data and the description of typhoon case

In this study, T-TREC-retrieved winds are used as the radar wind data. T-TREC technique retrieves the horizontal circulations of TCs from single Doppler radar reflectivity and V_r . The quality controlled radar data are interpolated to constant altitudes and then mapped onto polar coordinates centered at the TC. As an enhancement to the original TREC method (Tuttle and Gall 1999; Harasti et al. 2004), Doppler radial velocity is used to provide a constraint on the searching range for spatial correlation. Along with the reflectivity correlation coefficient calculated from two consecutive scan times, the velocity correlation coefficient is created from the radial velocity and the total correlation coefficient defined as the product of the two coefficients is used to determine the target cell (Wang et al., 2011). The wind vector is then estimated by the arc length between the initial and target cells and their time interval. The estimated winds are interpolated back onto the Cartesian grid in the end. In this study, radar data from two consecutive times at an interval of 6 minutes are used. For more details of T-TREC retrieval, please refer to Wang et al. (2011) and Li et al. (2013). The final resolution of T-TREC winds are 10 km horizontally and 1 km vertically. The typhoon case in this paper and its related T-TREC retrieved winds are summarized as follows.

Typhoon Chanthu (2010) formed as a tropical depression on the South China Sea on 18 July 2010, and intensified to a tropical storm by 1200 UTC, 19 July. The storm turned northwestward and strengthened to typhoon intensity by 1800 UTC, 21 July. The assimilation time is chosen at 1800 UTC, 21 July, when Chanthu moved into the full coverage of Haikou radar (HKRD) and the T-TREC winds retrieved from HKRD could provide the complete TC circulations (Fig. 3a). For the S-band radar used, the maximum coverage of reflectivity is 460 km which is much larger than the coverage of radial velocity, which is 230 km. Thus, the T-TREC-retrieved winds have a larger coverage than radial velocity from HKRD. The T-TREC winds at 3-km height are projected onto the HKRD radial direction (Fig. 3c) and compared with the observed V_r (Fig. 3d). Within the coverage of V_r (Fig. 3d), the projected T-TREC winds show similar pattern with the observed V_r suggesting the good quality of retrieval. The root mean square difference (RMSD) is only 2.7 m s^{-1} (Fig. 3b). Besides, the projected T-TREC winds show more complete velocity dipole pattern than V_r due to its larger coverage (Wang et al. 2011, 2014; Li et al. 2013). At 0600 UTC, 22 July, Chanthu finally made landfall at the city of Wuchuan, Guangdong province. The maximum surface wind (MSW) and MSLP before landfall reached 41 m s^{-1} and 963 hPa, respectively, according to Joint Typhoon Warning Center (JTWC) best track data. After bringing heavy rainfall to Guangdong and Guangxi provinces, the storm weakened to tropical depression on 23 July.

b. The WRF model configuration

The Advanced Research WRF (ARW) model (Skamarock et al. 2008) with full physics is used in this study. The forecasting domain is configured with 463×463 horizontal grid points with a 4-km grid spacing, and 35 levels in the vertical direction from the surface to 50 hPa. The physics options include the Purdue Lin scheme for microphysics processes, Monin-Obukhov surface-layer, Noah land-surface, YSU (Yonsei university) planetary boundary layer, Rapid Radiative Transfer Model (RRTM) longwave radiation, and Dudhia shortwave radiation schemes (Skamarock et al. 2008).

c. The data assimilation setup

The NCEP (National Centers for Environmental Prediction) operational GFS (Global Forecast System) analyses with 0.5° spacings are used to provide the unperturbed initial condition and the lateral boundary conditions. To examine the impact of the dynamic constraint within the 3DVar and En3DVar frameworks, five basic experiments, namely NoDA, 3DVAR, 3DVAR-DC, En3DVAR and En3DVAR-DC, are designed (Table 1). Reference experiment, NoDA, does not assimilate any additional data. Experiments 3DVAR and En3DVAR use the standard WRF 3DVar and En3DVar hybrid formulations, both assimilating radar T-TREC data. In experiment En3DVAR, ensemble covariance is used at 100% without any static covariance. Experiment 3DVAR uses only static covariance. In addition, we also conducted an experiment that used a 50% weighting for both ensemble and static error covariances. The analysis increments, the resulting track and intensity forecasts of this experiment are closer to those of 3DVAR, similar to the finding of Li et al. (2012). Li et al. (2012) also found that the use of 100% ensemble covariance gave best results. Therefore, we focus on the comparison of the results with 100% ensemble covariance with those of 3DVAR with pure static covariance in this paper. Experiments 3DVAR-DC and En3DVAR-DC are the same as experiments 3DVAR and En3DVAR, respectively, except for the inclusion of the additional dynamic constraint.

In all of our DA experiments, radar data is assimilated at a single time, and 40 members of 12-hour ensemble forecasts are initialized 12 hours prior to the analysis time. Ensemble members between 30 and 50 are most commonly used in EnKF and ensemble-hybrid data assimilation studied (e.g., Li et al. 2012; Zhu et al. 2013; Pan et al. 2014). Forty members were used in all of these three referenced studies, and represent a good compromise between costs and accuracy. Besides, the length of the pre-ensemble forecasts should be chosen so that the forecast are not too long for the forecast errors to become too large but not so short that flow-dependent error structures had no time to develop. Under such constraints, we choose to use 12 hours for the ensemble forecast spinup. Similar choices had been used in similar previous studies (e.g., Zhang et al. 2009; Weng and Zhang 2011). In the En3DVar experiments, the ensemble flow-dependent covariance is derived from these ensemble forecasts, while the analysis background is provided by the forecast ensemble mean. For consistency, the 3DVar experiments use the same analysis background. A 24-hour deterministic forecast is launched from each of the analyses while the forecast in NoDA continues from the analysis time without assimilating any data.

The initial conditions of the ensemble forecasts at 0600 UTC, 21 July are generated by adding correlated random perturbations to the GFS analysis. The random-cv (Barker 2005) facility (option ‘cv5’) in the WRF-3DVar system is used to create the perturbations following Torn et al. (2006), Wang et al. (2008a,b) and Zhang et al. (2009), and similar perturbations are also added to the boundary conditions. Based on the NMC-derived background error statistics, the perturbations have standard deviations of 1.5 m s^{-1} for the horizontal wind components, 0.7 K for temperature, 0.3 hPa for pressure perturbation, and 0.8 g kg^{-1} for water vapor mixing ratio.

Within the assimilation process for all DA experiments, the standard deviations of the observational errors for T-TREC winds are prescribed to be 4 m s^{-1} , according to the statistics of data samples (Wang et al. 2011). For 3DVAR/3DVAR-DC, similar to that used in Li et al. (2012) or Li et al. (2013), the spatial correlation length scale of static covariance is reduced by a factor of 0.25, in order to reflect the reasonable TC circulation increment. Li et al. (2012) showed that for the analysis of radar data for a TC, the use of the default spatial correlation scale given by the NMC-method-derived static covariance in WRF 3DVar produces spurious circulation increments. For En3DVAR/En3DVAR-DC which uses ensemble covariance, the localization radius of 50 km

in horizontal and 4 km in vertical are used, respectively. These choices are similar to those of Li et al. (2012) and Wang et al. (2014) and had been found to produce the best results for similar applications. Results using horizontal localization radius ranging from 20 to 200 km with the current application were reported in Li (2014); 50 km was found to be the best choice.

In addition, due to the nonlinearity of the added dynamic constraint, the outer loop (Courtier et al. 1994; Veerse and Thepaut 1998) procedure in assimilation is necessary in 3DVAR-DC/En3DVAR-DC. The outer loop updates the first guesses of each loop so that better initial state is provided for linearization minimization (inner loop), and thus benefit the quality of analysis. The number of outer loop is typically 2 to 6 (Massart et al. 2010; Hsiao et al. 2012; Sun and Wang 2013). In this study, we use 5 outer loops in our experiments.

Dimensional analysis is used to help determine the dynamic weight. In the dynamic equation $G(\mathbf{x})$, the advection and pressure gradient terms are dominant. For TC systems, the horizontal characteristic scale $L \sim 10^5$ m, the square of wind speed $U^2 \sim 10^3 \text{m}^2 \text{s}^{-2}$, and the pressure gradient $\Delta p \sim 10^3 \text{Pa}$. Thus, the magnitude of $G(\mathbf{x})$ is 10^{-2} . That is, if the dynamic weight Γ^{-1} is set to 10^4 , the dynamic constraint term will have a similar order of magnitude as the observation term. For the basic DA experiments 3DVAR-DC and En3DVAR-DC, we choose a dynamic weight of 10^3 so that the constraint term plays an important but not dominant role. Figure 2 shows that after 30 or so iterations, the observation and constraint terms are indeed of a similar order of magnitude (with the constraint term being several times smaller). In two additional sets of sensitivity experiment, this weight is increased or decreased by a factor of 4 or 16, corresponding to En3DVAR-DCi4, En3DVAR-DCi16, and En3DVAR-DCd4 and En3DVAR-DCd16, respectively.

4. Results

In this section, the results of initialization and subsequent forecasts for typhoon Chanthu (2010) from experiments NoDA, 3DVAR, 3DVAR-DC, En3DVAR and En3DVAR-DC are evaluated. The differences in the analyzed TC structures among different assimilation experiments are discussed in section 4a while the results of subsequent deterministic forecasts are examined in section 4b.

a. Results of analysis from assimilation experiments

In Fig. 4, we first present the background field at 1800 UTC, 21 July, which is provided by the mean of 12-h ensemble forecasts. It reveals that the background vortex circulation at the 3-km height is weak with a broad eye (Fig. 4a) and no obvious warm core is found in the southwest-northeast vertical cross section of horizontal wind speed and potential temperature (Fig. 4b). Besides, the MSLP from ensemble mean is only 994 hPa.

Figure 5 shows the increments of horizontal winds at 3-km height after analyzing T-TREC winds at 1800 UTC for experiments 3DVAR, 3DVAR-DC, En3DVAR and En3DVAR-DC. It is shown that, within the T-TREC wind coverage, the single-time assimilation produces clear cyclonic incremental circulations around the observed typhoon center, resulting in a much stronger vortex with a maximum wind speed increment exceeding 25m s^{-1} in all of the DA experiments (Figs. 5a-d). The increments from the En3DVar experiments are mostly found in or near the areas of data coverage. Clearly noticeable anti-cyclonic incremental circulation is, however, also found in the 3DVar experiments (Figs. 5a, b) in the northwest quadrant of the TC, with the circulation being weaker in the experiment that includes the dynamic constraint (Fig. 5b). Such structures are

common in WRF-3DVar analyses of TCs when assimilating radar wind observations (e.g., Fig. 6 of Li et al. 2012) and are unphysical. As suggested by Xie et al. (2012) and Sun and Wang (2013), this behavior is related to the use of stream function and velocity potential (ψ and χ , which are associated with the non-divergent rotational flow and divergent flow, respectively) as the control variables for the horizontal flows in the 3DVar and the assumption that the flow is dominated by the non-divergent, stream function component of flow, as reflected in the background error statistics obtained from the NMC method; the background error standard deviation of stream function ψ is generally much larger than that of velocity potential χ . With the flow-dependent ensemble covariance used in the En3DVar experiments, no prior assumption is made about the error variances associated with rotation and divergence flow components. In fact, in 3DVar systems that employ the Cartesian wind components (u , v) as the control variables, including the ARPS 3DVar system (Gao et al. 2004), no similar problem occurs. This can be seen from Fig. 4 of Zhao et al. (2012a, b) that assimilated radar data for TCs using the ARPS 3DVar system; no anti-cyclonic analysis increments were found their analysis increments.

Since the assimilated radar data provide direct information on the wind field only, the pressure field is adjusted through cross-covariance between wind and pressure and/or the linkage provided by the included dynamic constraint. Figure 6 shows the sea level pressure (SLP) increments from the four basic DA experiments. The smallest SLP increment of less than -2 hPa is found in experiment 3DVAR (Fig. 6a). The smallness of the increment is attributed to the weak multivariate correlation between wind and surface pressure in the static covariance which only reflects the approximate geostrophic wind balance. Although 3DVAR-DC has a larger SLP increment of about -4 hPa (Fig. 6b) which benefited from the dynamic constraint reflecting approximate gradient wind balance, it is still too small (the MSLP is more than 20 hPa too high in the background). In both 3DVAR and 3DVAR-DC cases, the pressure increments are rather broad. In comparison, the negative increments produced by En3DVAR and En3DVAR-DC are much more concentrated near the typhoon center (Figs. 6c, d), and are -8 and -13 hPa, respectively. There is also some increase in pressure surrounding this core of negative pressure increment.

The pressure increments of both larger and smaller scales in the En3DVar experiments indicate a better representation of the flow-dependent background error covariance, especially the cross-covariance between wind and surface pressure, associated with the typhoon, as estimated from the ensemble forecasts. The even larger increment in En3DVAR-DC reflects the stronger linkage between the wind and pressure fields in the inner core region through the equation constraint, and it matches the strong cyclonic wind increments found in the experiment (Fig. 5d). The combination of dynamic constraint and flow-dependent cross-variable covariance linking the observed wind and unobserved pressure produces more dynamically consistent analysis fields.

After examining the increment fields, we now show in Fig. 7 the total analyzed SLP and surface wind fields. By a single-time analysis, the MSLP in 3DVAR is 994 hPa (Fig. 7a), which is much higher than the best track data of 970 hPa. The surface circulation center is slightly displaced from the observed typhoon center but the center of minimum pressure is further displaced from the circulation center, creating a mis-match between the pressure and wind patterns (Fig. 7a). Including the dynamic constraint, the vortex circulation is better matched with the pressure pattern in 3DVAR-DC (Fig. 7b), while the MSLP is 2 hPa lower than in 3DVAR. The pressure pattern also matches that of wind well in both En3DVAR and En3DVAR-DC, indicating the dynamically consistent cross-covariance between wind and pressure used in the two cases, and the further positive help from the dynamic constraint in En3DVAR-DC (Figs. 7c, d). The MSLP in En3DVAR-DC reaches 983 hPa (Fig. 7d), which has the smallest MSLP error verified against

the best track data. Meanwhile, the tightest surface vortex circulation is found in En3DVAR-DC, among all the DA experiments. The results again show the benefit of flow-dependent background error covariance and the dynamic constraint when assimilating radar wind measurements. .

To compare the vertical structures of the analyzed TC, a southwest-northeast vertical cross section of horizontal wind speed and potential temperature through the analyzed TC center at the surface is plotted in Fig. 8 for each experiment. Compared to the background (Fig. 4b), the vortex circulations in all DA experiments are much stronger and clearly show the eyewall structures extending from surface to about 10-km height. The surface winds in 3DVAR and 3DVAR-DC are not as much influenced by radar winds at higher levels (radar data do not reach the surface due to the non-zero elevation of the lowest scan) owing to limited vertical spatial correlation in the static covariance, which is a major reason for the rather small SLP increment in 3DVAR-DC (Fig. 6b), even with the use of the dynamic constraint. For the En3DVar experiments, the analyzed winds show more asymmetric structures than those in 3DVar experiments, because the flow-dependent covariance contains spatially inhomogeneous information. Note that in experiments 3DVAR and En3DVAR (Figs. 8a, c) which exclude the dynamic constraint, the magnitudes of winds are somewhat larger than those in 3DVAR-DC and En3DVAR-DC (Figs. 8b, d), respectively. However the relatively larger wind speeds in 3DVAR/En3DVAR are not accompanied by lower minimum pressure expected (Figs. 7a, c) compared to those in 3DVAR-DC/En3DVAR-DC (Figs. 7b, d). These results again suggest that the analysis fields are more dynamically balanced when the constraint is included due to the mutual adjustment between wind and pressure.

The downward bending of isentropes in En3DVAR and En3DVAR-DC indicates warm core structures within the TC throughout the troposphere. The maximum of the warm core structure is found near 10-km height, consistent with the rapid decrease of wind speed above 10-km (Figs. 8c, d) according to thermal wind balance. However, in 3DVAR and 3DVAR-DC, weak warm core structure is only found above 11-km height, the potential temperature contours are nearly straight in the lower levels. The results indicate that the temperature field is also better analyzed in En3DVar and, En3DVAR-DC experiments, and the analyzed TC is dynamically and thermodynamically more balanced.

To better illustrate the additional benefit of including the dynamic constraint in En3DVAR-DC, we show in Fig. 9 the differences in the analyzed pressure, potential temperature and water vapor mixing ratio fields of En3DVAR-DC from those of En3DVAR, which are not directly observed. In the southwest-northeast vertical cross section shown, the additional pressure reduction in En3DVAR-DC extends throughout the troposphere but decreases with height (Fig. 9a). Consistently, the potential temperature in the vortex center is increased especially at the lower levels (Fig. 9b) where the pressure increment is the largest. The moisture field is also generally increased near the vortex center throughout the troposphere (Fig. 9c), with the largest increment at the surface. All of these show a positive impact of including the dynamic constraint on the analysis of the TC structures.

b. Impact of data assimilation on TC forecast

The impacts of assimilating the radar wind data using different DA schemes are further evaluated by examining the subsequent deterministic forecasts launched from the analyses. The predicted typhoon tracks, track errors, MSLPs and MSWs of 24-h forecasts from the four DA experiments as well as experiment NoDA are plotted in Fig.10, as verified against the Joint Typhoon Warning Center (JTWC) best track data. Without radar assimilation, NoDA has an initial track error of about 65 km (Fig. 10b). In comparison, all DA experiments are able to reduce the

initial track errors, indicating the ability of radar DA in correcting the initial TC position error. Experiment 3DVAR has a relative higher initial track error among the four DA experiments of about 55 km since the SLP only has limited adjustment (Fig. 6a) and the MSLP center is not relocated much by the analysis (Fig. 7a) (in this study, we determine the TC track based on the MSLP location). Among all, En3DVAR-DC gives the smallest initial track error of about 10 km, which can also be seen from Fig. 7. During the forecasting period, Chanthu maintained a northwest track before and after landfall. In NoDA, the predicted storm first took a more northward track in the first 6 hours. The northward bias results in its landfall at 0000 UTC, 22 July further eastward along the southern coast, earlier than the observed landfall time of 0600 UTC. After that, the storm moves northwestward until 0900 UTC and then turns further southwestward, resulting in a 24-h mean track error of 80 km (Fig. 10b). For the four DA experiments, generally, the predicted tracks show mostly northwestward trend. However, the tracks in 3DVAR and 3DVAR-DC show much more northward biases between 6 and 12 hours, resulting in 24-h mean errors of 75 km and 68 km, respectively. The too much northward component can be attributed to the believed-to-be-spurious south wind increments in the northwest part of the storm analyzed by the 3DVar (Figs. 5a, b). This is a common problem with the WRF 3DVAR when analyzing radar winds, as was discussed earlier. We also tried one additional experiment in which the negative incremental structure around the edge of radar data coverage region in experiment 3DVAR is artificially eliminated, the predicted typhoon track shows more correct trends (not shown). In comparison, En3DVAR and En3DVAR-DC show better predicted tracks that are closer to the best track, with the mean errors being 31 km and 33 km, respectively. The similarity in the track errors of En3DVAR and En3DVAR-DC suggests that the added dynamic constraint has more impact on the analyzed intensity and structures of the typhoon than on track forecast. The better horizontal circulation structures obtained in the En3DVar experiments seem to have larger impacts on the track forecast.

The observed typhoon starts from about 970 hPa of MSLP and 36 m s^{-1} of MSW with the intensity increasing to 963 hPa and 41 m s^{-1} until 0000 UTC, 22 July and then weakens due to landfall (Figs. 10c, d). NoDA underestimates the intensity during the forecasting period in both MSLP and MSW, owing to the too weak initial vortex (Fig. 4). All DA experiments show improvement over NoDA with intensity trends more similar to those of best track (Figs. 10c, d). For 3DVAR and 3DVAR-DC, the MSLPs start from 994 and 992 hPa, respectively, and deepen to 980 and 979 hPa before landfall at 0300 UTC, 22 July. On average, the predicted MSLPs are higher than the best track, leading to mean MSLP errors of 11.2 hPa and 9.8 hPa, respectively. The mean errors of predicted MSWs for 3DVAR and 3DVAR-DC are 4.8 m s^{-1} and 4.5 m s^{-1} , respectively. The predicted MSLP and MSW undergoes marked adjustment during the first hour in 3DVAR and 3DVAR-DC, with rapid decrease in MSLP and rapid increase in MSW, indicating large initial imbalance the analyzed wind and pressure. For En3DVAR and En3DVAR-DC, the mean MSLP (MSW) errors are 8.3 hPa (4.4 m s^{-1}) and 6.9 hPa (4.1 m s^{-1}), respectively, clearly better than corresponding 3DVar experiments. Initial adjustments are also found in the first hour but they are much smaller than those in the 3DVar experiments. The predicted MSLPs in the two experiments reach the minimum values of 976 hPa and 974 hPa before landfall, respectively. This is consistent with the fact that the En3DVar experiments are able to better build up the warm core structure (Fig. 8c, d) which can induce lower central pressure in the forecasts. Besides, the predicted MSLPs in En3DVAR-DC are lower than those in En3DVAR throughout the forecasting period. En3DVAR and En3DVAR-DC also forecast higher MSWs than 3DVAR and 3DVAR-DC, especially in the first 6 hours before landfall, with those of En3DVAR-DC being closest to the best track.

Because the MSW is sensitive to local wind speed variations, we further plot the azimuthal mean tangential winds for all experiments at 0300 UTC, 22 July (9-h forecasting time) are plotted in Figure 11a-e, together and the azimuthal mean temperature deviations from the horizontal mean. For comparison, retrieved tangential winds from radar radial velocity observations of HKRD using the GBVTD technique (Lee et al. 1999) are displayed in Fig. 11f. Improving over NoDA (Fig. 11a), all DA experiments produce much better defined eyewall structures. The GBVTD retrievals show that the maximum winds are located at a radius of about 40km. The En3DVar experiments (Fig. 11d, e) show more compact circulations with smaller RMWs (radius of maximum wind) of 40 km, better than those of 3DVar experiments (Fig. 11b, c). Among all, En3DVAR-DC exhibits the most intense eyewall structures with a maximum mean wind speed of 37 m s^{-1} around 1-km height which is comparable to the 39 m s^{-1} of GBVTD retrieval. Along with the strongest vortex circulation, the maximum temperature anomaly exceeding 8 K at about 7-km height in En3DVAR-DC is larger than those of other experiments. An inadequate aspect is that the predicted storms in all DA experiments tend to under-estimate the wind speed above 2-km height.

We next evaluate the predicted reflectivity structures. Figures 12 and 13 show the predicted column-maximum radar reflectivity and horizontal wind vectors at the 3-km height from NoDA, 3DVAR, 3DVAR-DC, En3DVAR and En3DVAR-DC, together with the observed composite reflectivity at 0000 UTC, 22 July (6 hours of forecast time and before landfall) and 0600 UTC, 22 July (at landfall), respectively. At 0000 UTC, typhoon Chanthu was located on the east side of Leizhou Peninsula and Hainan Island (Fig. 12f). In NoDA, the vortex is weak and the predicted reflectivity eyewall around the inner core is mostly missed (Fig. 12a). 3DVAR and 3DVAR-DC (Fig. 12b, c) show better organized vortices, but the eyes are still broader than observed. In comparison, En3DVAR and En3DVAR-DC produce tighter vortices and better-defined eyewalls with strong echoes located in the southeast quadrant as observed (Figs. 12d, e). The smallest weak reflectivity hole at the typhoon center is found in En3DVAR-DC, close to the observed eye. However, the predicted typhoon location has some northward bias (Fig. 12e). The main imperfect aspect of all DA experiments is that the observed outer rainbands located on the northeast side of the typhoon are mostly missing or are located too far out.

At the landfall time of 0600 UTC, 22 July, the observed precipitation pattern becomes more asymmetric. The northern half of the storm is less fueled by moist air due to landfall and the strong echoes are found only on the south side near Leizhou Peninsula (Fig. 13f). All the DA experiments again show better predicted reflectivity with better organized eyewall structures than NoDA (Fig. 13a). 3DVAR and 3DVAR-DC produce more symmetric eyewalls with broader eyes than observed, and the predicted typhoon has much eastward bias (Figs. 13b, c). In contrast, En3DVAR and En3DVAR-DC compare more favorably with radar observations with better TC position and tighter vortex circulation (Figs. 13d, e). The highly asymmetric eyewall structure is captured well to some extent, together with a small weak reflectivity hole in En3DVAR-DC (Fig. 13e).

Overall, the En3DVar experiments produce better predicted reflectivity pattern than those of NoDA, 3DVAR and 3DVAR-DC. Although the differences in the predicted structures between En3DVAR and En3DVAR-DC are small, En3DVAR-DC actually produces a more compact storm with a tighter eye, closer to radar observations. It is also worth pointing out that all the experiments tend to over-predict the reflectivity as compared to the observation. This is most likely due to deficiencies in the microphysics parameterization. As mentioned in Rogers et al. (2007), the magnitude of peak reflectivity is often higher in numerical simulations than observations by 10-15 dBZ. Similar over-prediction of reflectivity is also found in Zhang et al. (2009) and Ming et al. (2012) for TCs and the solution to this problem is beyond the scope of this study.

Figure 14 shows the 24-h accumulated precipitation and the corresponding equitable threat scores (ETS) for all experiments along with the high-resolution automatic weather station rainfall measurements. 1625 automatic weather stations are used and their spatial distributions are presented in Fig. 14f. The observed heavy rainfall is mostly distributed at the southwest corner of Guangdong Province and the north part of Leizhou Peninsula. The maximum center is located near Zhanjiang City (see Fig. 3a for locations) and the 24-h precipitation exceeds 300 mm (Fig. 14f). NoDA clearly misses the intense observed precipitation areas and clearly over-predicts the rainfall in Guangxi Province (Fig. 14a), which is attributed to its poor track forecast after landfall (Fig. 10a). The areas of heaviest rainfall in 3DVAR and 3DVAR-DC are located too far east (Figs. 14b, c), mainly owing to their eastward track biases. As a result, the ETS scores for 3DVAR are only 0.18, 0.13 and 0.02 for the 80 mm, 120 mm and 160 mm thresholds, respectively. 3DVAR-DC is slightly better, with the ETS scores being 0.26, 0.15 and 0.02 for the 80 mm, 120 mm and 160 mm thresholds. In comparison, experiments En3DVAR and En3DVAR-DC show much better intensity and coverage in precipitation forecasts. Heavy precipitation in northern Leizhou Peninsula is well captured although there is a somewhat westward bias over the continent, and more so for En3DVAR (Fig. 14d). The ETS of En3DVAR are 0.48, 0.33 and 0.17 for the three thresholds, respectively, while En3DVAR-DC gets higher ETS scores of 0.51, 0.32 and 0.23. Overall, although all DA experiments tend to under-predict the magnitudes of precipitation at the observed maximum regions, En3DVAR-DC generally produces the best precipitation forecast according to the ETS scores, which benefited from its improved track, intensity and structure forecasting of the landfalling typhoon.

5. Sensitivity experiments

The above experiments have shown positive impacts of including the dynamic constraint in the En3DVar scheme. In this section, we want to see whether the behaviors depend on the choice of the weight for the dynamic constraint term because its choice is empirical. Sensitivity experiments are performed to investigate this issue, as described in section 3. For brevity, we only present the analyzed fields for En3DVAR-DCi16/En3DVAR-DCd16 (Fig. 15) which increases/decreases the default value of the dynamic weight by a factor of 16, while the predicted track and intensity results from all sensitivity experiments (Table. 1) are shown in Fig. 16.

Figure 15 shows the analyzed TC structures of En3DVAR-DCi16 and En3DVAR-DCd16 at 1800 UTC, 21 July. The analyzed MSLP in En3DVAR-DCi16 and En3DVAR-DCd16 are about 986 hPa and 987 hPa, respectively. The value of 987 hPa in En3DVAR-DCd16 is between those of 988 hPa and 983 hPa in En3DVAR and En3DVAR-DC. It suggests that the decreased dynamic weight results in less impact of the constraint term, which is not surprising. It is, however, somewhat surprising that the MSLP value of 986 hPa in En3DVAR-DCi16 is not as low as that of 983 hPa in En3DVAR-DC. The stronger dynamic constraint in En3DVAR-DCi16 is expected to cause more adjustment in pressure than in En3DVAR-DC. To understand this behavior, southwest-northeast vertical cross sections of horizontal wind speeds through the TC center are plotted in Figs. 15c,d for En3DVAR-DCi16 and En3DVAR-DCd16, respectively. The cross section plotted is the same with those in Fig. 8. The analyzed horizontal wind speeds at all levels in En3DVAR-DCi16 are obviously smaller than those in En3DVAR-DC. It is attributed to the fact that the higher value of dynamic weight plays a role in assigning relatively more weight to the constraint term than the observation term. The reduced relative impact of the observation term leads to smaller wind increments from the radar T-TREC wind data. The weaker analyzed vortex circulations in

En3DVAR-DCi16 result in a higher MSLP than in En3DVAR-DC. In En3DVAR-DCd16, the magnitude of horizontal wind speeds is closer to that of En3DVAR, than that of En3DVAR-DC, because of the weaker constraint. These sensitivity experiments indicate there are optimal values for the weight where the constraint term has the largest impacts.

Figure 16 shows the predicted track, track errors, MSLP errors and MSW errors for all four sensitivity experiments, as well as for En3DVAR and En3DVAR-DC. Generally, for track and intensity forecasting, increasing the dynamic weight relative to the control value has larger negative impacts than decreasing the weight. When the weight is increased by a factor of 16, the MSLP and MWS errors are much larger (Figs. 16c, d). It indicates that one should be cautious in choosing very large values for the dynamic weight, which can degrade the analysis and subsequent intensity forecast. Generally, within a reasonable range, the dynamic constraint is effective in adjusting the pressure field towards the wind field constrained by the radar wind observations. The results also suggest that the value of 10^3 used in the basic experiments specified with the help of dimensional analysis is close to optimal in our case.

6. Summary and conclusions

In this study, a dynamic equation constraint based on the steady momentum equations is incorporated into the WRF hybrid ensemble-3DVar (En3DVar) DA system as a weak constraint in the cost function. The constraint aims at improving the coupling and balance among wind and other state variables, especially when few state variables are directly observed. Such a constraint can be especially helpful when analyzing for tropical cyclones where the wind and pressure fields in the inner core region are in approximate gradient balance.

The scheme is applied to the assimilation of radar T-TREC (Typhoon-Tracking Radar Echo by Correlation) winds at a convection-allowing 4 km grid spacing for landfalling typhoon Chanthu (2010) when it was within the range of a coastal operational radar. The impact of the equation constraint on the analysis and forecast of Chanthu is evaluated first through a set of four basic DA experiments where the hybrid DA system either used pure static 3DVar background error covariance (with experiments named 3DVAR and 3DVAR-DC, where DC denotes dynamic constraint) or pure ensemble-derived flow-dependent error covariance (experiments En3DVAR and En3DVAR-DC). The T-TREC wind data are assimilated at a single time to highlight the direct effects of DA. Dimensional analysis is used to help determine the suitable values for the weight of the dynamic constraint term. The results of analyses and subsequent forecasts from the DA experiments, and an experiment where no radar data is assimilated (NoDA), are verified against available radar observations and best track data.

The single-time assimilation of T-TREC-retrieved winds results in enhanced vortex circulations in all DA cases. The wind increments in the En3DVar cases are mostly concentrated in the core regions of the vortex giving better analyzed vortex center locations, and the wind increments decrease away from the vortex core where radar data coverage also disappears. However, unrealistic, generally anti-cyclonic wind increments are found away from the core region, outside the radar coverage areas when the scheme becomes the standard 3DVar with pure static covariance. Overall, En3DVar with the dynamic constraint gives the best analysis of center location and vortex intensity in terms of both minimum sea-level pressure and maximum surface wind.

From the vertical cross sections, more asymmetric structures are obtained in the analysis in the En3DVar experiments with ensemble-derived covariance. The dynamic constraint is much

more effective in En3DVAR-DC where radar measured wind information is better propagated to the surface due to better vertical spatial covariance, producing larger surface wind as well as pressure increments. The better analyzed pressure field is also accompanied by better temperature and moisture analyses in En3DVar-DC, which is more due to the flow-dependent cross-covariances, resulting in more dynamically and thermodynamically balanced analysis fields.

For the subsequent forecasts, all four DA experiments improve the intensity (MSLP and MSW) forecasts considerably compared to NoDA experiment. Among all the experiments, the En3DVar scheme with dynamic constraint shows the best intensity forecast, especially in terms of MSLP, consistent with the best analysis of MSLP. The En3DVar experiments with flow-dependent covariance (En3DVAR and En3DVAR-DC) yield better track forecasts compared to 3DVar experiments 3DVAR and 3DVAR-DC. Besides, the En3DVar experiments, especially En3DVAR-DC, tend to predict more compact vortices with a tighter eye that is closer to observed. For 24-h accumulated precipitation, En3DVAR-DC also produces the best forecast when verified against automatic weather station rainfall measurements, in terms of both visual pattern and ETS scores.

Additional En3DVar sensitivity experiments were performed in which the weight for the dynamic constraint is increased or decreased by a factor of 4 or 16, relative to the weight used in En3DVAR-DC. The decreased weights lead to slightly higher analyzed MSLP values due to the weaker coupling between wind and pressure. Further increasing the dynamic weight actually has larger negative impact on the analyzed MSLP, and this is apparently due to the reduced relative weight of the observation term and reduced wind increments. As a result, the vortex is weaker in terms of both wind circulation and pressure pattern. The default value of 10^3 for the weight of the constraint used in control experiment En3DVAR-DC appears optimal, and the results are not very sensitive to the weight as long as the value is not too far from the optimal value.

This study mainly serves the purpose of testing and evaluating a dynamic equation constraint newly implemented within the WRF En3DVar hybrid DA system based on the steady state momentum equations, and to see how the constraint helps improve the analysis of landfalling TCs when the available data are from a coastal Doppler radar, in particular for the analysis of the pressure field. Although the results are clearly encouraging, the system should be evaluated with more TC cases for more robust conclusions. Future, the inclusion of additional radar data assimilation cycles should help future improve the analysis of the TCs. The system should also benefit from better background forecasts that may be obtained through cycled ensemble Kalman filter data assimilation during the pre-forecast period (before the T-TREC wind data are available). These are topics for further studies. Further, we note that the equation constraint implemented in this study should be generally applicable to problems where the wind and pressure fields are more or less in balance, such as in mesoscale scale convective vortex or other mesoscale connective systems, although its effectiveness for such systems will require further studies. Since the equations are implemented as weak constraints in the cost function, its weight can be further tuned for optimal results for general, potentially operational applications.

Acknowledgements: This work was primarily supported by National Fundamental Research 973 Program of China (2013CB430100 and 2015CB452801), the Social Common Wealth Research Program (GYHY201006007 and GYHY201206005), and the Chinese Natural Science Foundation (grants 41105035). We are grateful to the High Performance Computing Center of Nanjing University for doing the numerical calculations in this paper on its IBM Blade cluster system. And the observed data used in this study was collected by an experiment supported by the National Key Basic Research and Development Program of China (973 program: 2009CB421500). Because of

the data policy of 973 program, the data cannot be released until 2018. Before that one with special interest in the data used in this study can request by contacting the office of this 973 program through email: sunj@mail.typhoon.gov.cn.

References

- Anderson, J. L. (2001), An ensemble adjustment Kalman filter for data assimilation. *Mon. Wea. Rev.*, *129*, 2884–2903.
- Barker, D. M. (2005), Southern high-latitude ensemble data assimilation in the Antarctic Mesoscale Prediction System. *Mon. Wea. Rev.*, *133*, 3431–3449
- Bishop, C., B. J. Etherton, and S. J. Majumdar (2001), Adaptive sampling with the ensemble transform Kalman filter. Part I: Theoretical aspects. *Mon. Wea. Rev.*, *129*, 420–436.
- Buehner, M. (2005), Ensemble-derived stationary and flow dependent background-error covariances: Evaluation in a quasi-operational NWP setting, *Quart. J. Roy. Meteor. Soc.*, *131*, 1013–1043.
- Chen, Y. S., and C. Snyder (2007), Assimilating Vortex Position with an Ensemble Kalman Filter, *Mon. Wea. Rev.*, *135*, 1828–1845.
- Courtier, P., and O. Talagrand (1987), Variational assimilation of meteorological observations with the adjoint vorticity equation. II: Numerical results, *Quart. J. Roy. Meteor. Soc.*, *113*, 1329–1368.
- Courtier, P., J.-N. Thépaut, and A. Hollingsworth (1994), A strategy for operational implementation of 4D-Var, using an incremental approach, *Quart. J. Roy. Meteor. Soc.*, *120*, 1367–1387.
- Dong, J., and M. Xue (2013), Assimilation of radial velocity and reflectivity data from coastal WSR-88D radars using ensemble Kalman filter for the analysis and forecast of landfalling hurricane Ike (2008), *Q. J. R. Meteorol. Soc.*, *139*, 467–487.
- Evensen, G. (1994), Sequential data assimilation with a nonlinear quasigeostrophic model using Monte Carlo methods to forecast error statistics, *J. Geophys. Res.*, *99*(C5), 10143–10162.
- Gao, J.-D., M. Xue, A. Shapiro, and K. K. Droegemeier (1999), A Variational Method for the Analysis of three-Dimensional Wind Fields from Two Doppler Radars, *Mon. Wea. Rev.*, *127*, 2128–2142.
- Gao, J.-D., M. Xue, A. Shapiro, Q. Xu, and K. K. Droegemeier, (2001), Three dimensional simple adjoint velocity retrievals from single Doppler radar, *J. Atmos. Oceanic Technol.*, *18*, 26–38.
- Ge, G., J.-D. Gao, and M. Xue (2012), Diagnostic Pressure Equation as a Weak Constraint in a Storm-Scale Three-Dimensional Variational Radar Data Assimilation System, *J. Atmos. Oceanic Technol.*, *29*, 1075–1092.
- Hamill, T. M., and C. Snyder (2000), A hybrid ensemble Kalman filter-3D variational analysis scheme, *Mon. Wea. Rev.*, *128*, 2905–2919.
- Harasti, P. R., C. J. McAdie, P. P. Dodge, W. C. Lee, J. Tuttle, S. T. Murillo, and F. D. Marks (2004), Real-time implementation of single-Doppler radar analysis methods for tropical cyclones: Algorithm improvements and use with WSR-88D display data, *Wea. Forecasting*, *19*, 219–239.
- Houtekamer, P. L., and H. L. Mitchell (1998). Data assimilation using an ensemble Kalman filter technique. *Mon. Wea. Rev.*, *126*(3), 796–811.
- Hsiao, L. F., D. S. Chen, Y. H. Kuo, Y. R. Guo, T. C. Yeh, J. S. Hong, C. T. Fong, and C. S. Lee

- (2012), Application of WRF 3DVAR to Operational Typhoon Prediction in Taiwan: Impact of Outer Loop and Partial Cycling Approaches, *Wea. Forecasting*, 27, 1249–1263.
- Lee, W. C., B. J. D. Jou, P. L. Chang, and S. M. Deng (1999), Tropical cyclone kinematic structure retrieved from Single-Doppler radar observations. Part I: Interpretation of Doppler velocity patterns and the GBVTD technique, *Mon. Wea. Rev.*, 127, 2419-2439.
- Li, Y., X. Wang, and M. Xue (2012), Assimilation of radar radial velocity data with the WRF ensemble-3DVAR hybrid system for the prediction of hurricane Ike (2008), *Mon. Wea. Rev.*, 140, 3507-3524.
- Li, X., J. Ming, Y. Wang, K. Zhao, and M. Xue (2013), Assimilation of T-TREC-retrieved wind data with WRF 3DVAR for the short-term forecasting of typhoon Meranti (2010) near landfall, *J. Geophys. Res.*, 118, 10361–10375.
- Liu, Z., C. S. Schwartz, C. Snyder, and S.-Y. Ha (2012), Impact of assimilating AMSU-A radiances on forecasts of 2008 Atlantic tropical cyclones initialized with a limited-area ensemble Kalman filter. *Mon. Wea. Rev.*, 140, 4017–4034.
- Liang, X., B. Wang, J. Chan, Y. Duan, D. Wang, Z. Zeng, L. Ma (2007), Tropical cyclone forecasting with model-constrained 3D-Var. I: Description. *Q. J. R. Meteorol. Soc.* 133(622), 147 - 153.
- Lorenc, A. C. (2003), The potential of the ensemble Kalman filter for NWP—A comparison with 4D-VAR, *Quart. J. Roy. Meteor. Soc.*, 129, 3183–3203.
- Massart, S., B. Pajot, A. Piacentini, and O. Pannekoucke (2010), On the merits of using a 3D-FGAT assimilation scheme with an outer loop for atmospheric situations governed by transport, *Mon. Wea. Rev.*, 138, 4509–4522.
- Ming, J., S. Shu, Y. Wang, J. Tang, and B. Chen (2012), Modeling Rapid Intensification of Typhoon Saomai (2006) with the Weather Research and Forecasting Model and Sensitivity to Cloud Microphysical Parameterizations, *J. Meteor. Soc. Japan*, 90, 771–789.
- Pan, Y., K. Zhu, M. Xue, X. Wang, M. Hu, S. G. Benjamin, S. S. Weygandt, and J. S. Whitaker (2014), A regional GSI-based EnKF-variational hybrid data assimilation system for the Rapid Refresh configuration: Results with a single, reduced resolution. *Mon. Wea. Rev.*, 142, 3756-3780.
- Parrish, David F., John C. Derber (1992), The National Meteorological Center's Spectral Statistical-Interpolation Analysis System, *Mon. Wea. Rev.*, 120, 1747–1763.
- Pu, Z., X. Li, and J. Sun (2009), Impact of airborne Doppler radar data assimilation on the numerical simulation of intensity changes of Hurricane Dennis near a landfall, *J. Atmos. Sci.*, 66, 3351–3365.
- Rogers, R. F., M. L. Black, S. S. Chen, and R. A. Black (2007), An evaluation of microphysics fields from mesoscale model simulations of tropical cyclones. Part I: Comparisons with observations. *J. Atmos. Sci.*, 64, 1811–1834.
- Sasaki, Y. (1970a), Some basic formalisms in numerical variational analysis. *Mon. Wea. Rev.*, 98(12), 875-883.
- Sasaki, Y. (1970b), Numerical variational analysis formulated under the constraints as determined by longwave equations and a low-pass filter. *Mon. Wea. Rev.*, 98(12), 884-898.
- Sasaki, Y. (1970c), Numerical variational analysis with weak constraint and application to surface analysis of severe storm gust. *Mon. Wea. Rev.*, 98(12), 899-910.
- Schwartz, C. S., Z. Liu, Y. Chen, and Z. Hung (2012), Impact of assimilating microwave radiances with a limited-area ensemble data assimilation system on forecasts of Typhoon Morakot. *Wea. Forecasting*, 27, 424–437.

- Schwartz, C. S., Z. Liu, X.-Y. Huang, Y.-H. Kuo, and C.-T. Fong (2013). Comparing limited-area 3DVAR and hybrid variational-ensemble data assimilation methods for typhoon track forecasts: Sensitivity to outer loops and vortex relocation. *Mon. Wea. Rev.*, *141*, 4350–4372.
- Skamarock, W. C., J. B. Klemp, J. Dudhia, D. O. Gill, D. M. Barker, M. G. Duda, X.-Y. Huang, W. Wang, and J. G. Powers (2008), Description of the Advanced Research WRF version 4, Rep. NCAR/TN-475++STR, Natl. Cent. for Atmos. Res., Boulder, Colo.
- Sun, J., D. W. Flicker, and D. K. Lilly (1991), Recovery of three-dimensional wind and temperature fields from single-Doppler radar data, *J. Atmos. Sci.*, *48*, 876–890.
- Sun, J., and A. Crook (1994), Wind and Thermodynamic Retrieval from Single-Doppler Measurements of a Gust Front Observed during Phoenix II, *Mon. Wea. Rev.*, *122*, 1075–1091.
- Sun, J., and H. Wang. (2013), WRF-ARW Variational Storm-Scale Data Assimilation: Current Capabilities and Future Developments, *Advances in Meteorology 2013*, 1-13.
- Talagrand, O., and P. Courtier (1987), Variational assimilation of meteorological observations with the adjoint vorticity equation. I: Theory. *Quart. J. Roy. Meteor. Soc.*, *113*(478), 1311-1328.
- Torn, R. D., G. J. Hakim, and C. Snyder (2006), Boundary conditions for limited area ensemble Kalman filters, *Mon. Wea. Rev.*, *134*, 2490–2502.
- Tuttle, J., and R. Gall (1999), A single-radar technique for estimating the winds in tropical cyclones, *Bull. Am. Meteorol. Soc.*, *80*, 653-668.
- Veers éF., Thepaut J N. (1998), Multiple - truncation incremental approach for four - dimensional variational data assimilation, *Q. J. R. Meteorol. Soc.*, *124*(550), 1889-1908.
- Wang, X., C. Snyder, and T. M. Hamill, (2007), On the theoretical equivalence of differently proposed ensemble-/3DVar hybrid analysis schemes, *Mon. Wea. Rev.*, *135*, 222–227.
- Wang, X., D. Barker, C. Snyder, and T. M. Hamill (2008a), A hybrid ETKF–3DVAR data assimilation scheme for the WRF model, Part I: Observing system simulation experiment. *Mon. Wea. Rev.*, *136*, 5116–5131.
- Wang, X., D. Barker, C. Snyder, and T. M. Hamill (2008b), A hybrid ETKF–3DVAR data assimilation scheme for the WRF model, Part II: Real observation experiments. *Mon. Wea. Rev.*, *136*, 5132–5147.
- Wang, X., (2011), Application of the WRF hybrid ETKF-3DVAR data assimilation system for hurricane track forecasts, *Wea. Forecasting*, *26*, 868-884.
- Wang, M. J., K. Zhao, and D. Wu, (2011), The T-TREC technique for retrieving the winds of landfalling typhoons in China, *Acta Meteorol. Sin.*, *25*, 91-103.
- Wang, M., M. Xue, K. Zhao, and J. Dong (2014), Assimilation of T-TREC-retrieved winds from single-Doppler radar with an EnKF for the forecast of Typhoon Jangmi (2008), *Mon. Weather Rev.*, Accepted.
- Wang, H., J. Sun, X. Zhang, X. Huang, and Thomas Auligné (2013), Radar Data Assimilation with WRF 4D-Var. Part I: System Development and Preliminary Testing, *Mon. Wea. Rev.*, *141*, 2224–2244.
- Weng, Y., and F. Zhang (2012), Assimilating Airborne Doppler Radar Observations with an Ensemble Kalman Filter for Convection-Permitting Hurricane Initialization and Prediction: Katrina (2005), *Mon. Wea. Rev.*, *140*, 841-859.
- Xiao, Q., X. Zou, B. Wang (2000), Initialization and Simulation of a Landfalling Hurricane Using a Variational Bogus Data Assimilation Scheme. *Mon. Wea. Rev.*, *128*, 2252–2269.

- Xiao, Q., Y.-H. Kuo, J. Sun, W.-C. Lee, E. Lim, Y.-R. Guo, and D. M. Barker (2005), Assimilation of Doppler radar observations with a regional 3DVAR system: Impact of Doppler velocities on forecasts of a heavy rainfall case, *J. Appl. Meteorol. Climatol.*, *44*, 768–788.
- Xie, Y. and MacDonald, AE. (2012), Selection of Momentum Variables for a Three-Dimensional Variational Analysis, *Pure Appl. Geophys.*, *169*, 335–351.
- Xue, M., and J. Dong (2013), Impact of assimilating best track minimum sea level pressure data together with coastal Doppler radar data on hurricane analysis and prediction at a cloud-resolving resolution, *Acta Meteorol. Sin.*, *27*, 379-399.
- Zhang, F., Y. Weng, J. A. Sippel, Z. Meng, and C. H. Bishop (2009), Cloud-resolving hurricane initialization and prediction through assimilation of Doppler radar observations with an ensemble Kalman filter, *Mon. Wea. Rev.*, *137*, 2105-2125.
- Zhao, K., and M. Xue (2009), Assimilation of coastal Doppler radar data with the ARPS 3DVAR and cloud analysis for the prediction of Hurricane Ike (2008), *Geophys. Res. Lett.*, *36*, doi:10.1029/2009GL038658.
- Zhao, K., M. Xue, and W.-C. Lee (2012a), Assimilation of GBVTD-retrieved winds from single-Doppler radar for short-term forecasting of super typhoon Saomai (0608) at Landfall, *Q. J. R. Meteorol. Soc.*, *138*, 1055–1071.
- Zhao, K., X. Li, M. Xue, B. J.-D. Jou, and W.-C. Lee (2012b), Short-term forecasting through intermittent assimilation of data from Taiwan and mainland China coastal radars for Typhoon Meranti (2010) at landfall, *J. Geophys. Res.*, *117*, D06108, doi:10.1029/2011JD017109.
- Zhu, K., Y. Pan, M. Xue, X. Wang, J. S. Whitaker, S. G. Benjamin, S. S. Weygandt, and M. Hu (2013). A regional GSI-based EnKF system for the Rapid Refresh configuration: Results with a single, reduced resolution. *Mon. Wea. Rev.*, *141*, 4118-4139.

Table 1. Description of experiments

Experiments	Description	Background covariance	Dynamic constraint	Dynamic weight	Analyzed MSLP
NoDA	No radar data assimilation				
3DVAR	Assimilating T-TREC-retrieved winds at 1800 UTC, 21	Static	None	None	994 hPa
3DVAR-DC	Assimilating T-TREC-retrieved winds at 1800 UTC, 21	Static	Included	Default value of 10^3	992 hPa
En3DVAR	Assimilating T-TREC-retrieved winds at 1800 UTC, 21	Ensemble flow-dependent	None	None	988 hPa
En3DVAR-DC	Assimilating T-TREC-retrieved winds at 1800 UTC, 21	Ensemble flow-dependent	Included	Default value of 10^3	983 hPa
En3DVAR-DCd4	Similar with En3DVAR-DC			Decreased by 4	985 hPa
En3DVAR-DCd16	Similar with En3DVAR-DC			Decreased by 16	987 hPa
En3DVAR-DCi4	Similar with En3DVAR-DC			Increased by 4	984 hPa
En3DVAR-DCi16	Similar with En3DVAR-DC			Increased by 16	986 hPa

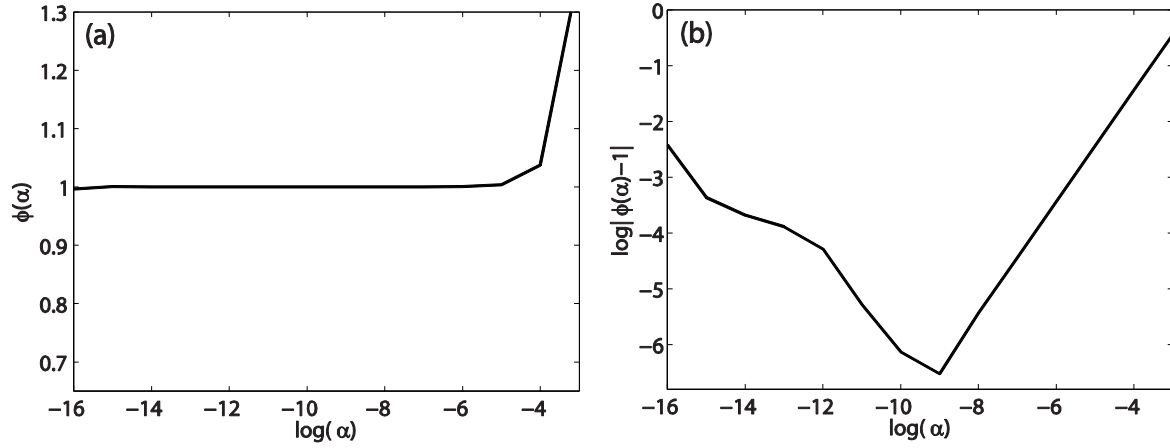


Fig. 1. Verifications of the gradient calculation: (a) variation of Φ with respect to $\log \alpha$; (b) variation of $\log(\Phi - 1)$ with respect to $\log \alpha$.

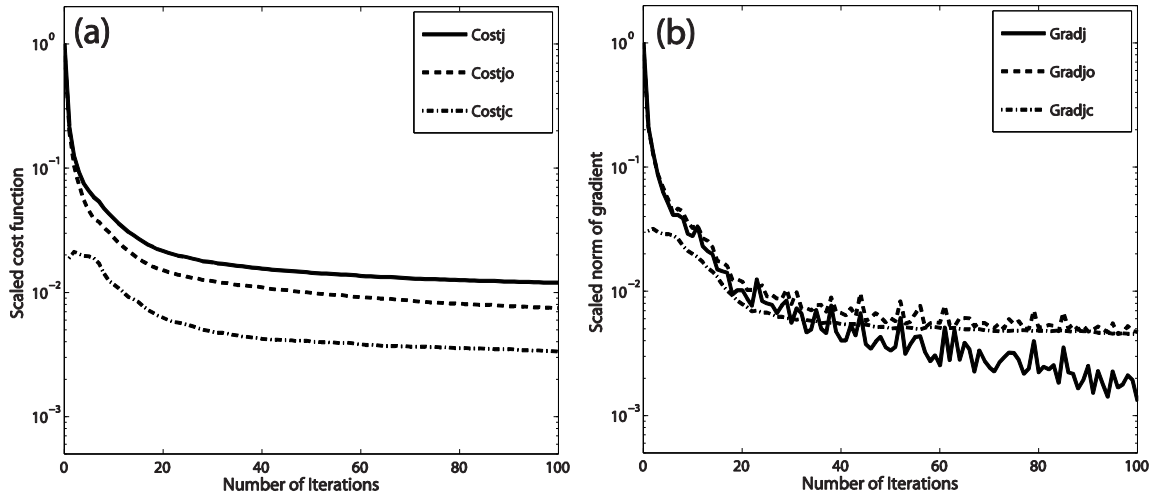


Fig. 2. The (a) scaled total cost function and (b) its norm of gradient as a function of the iteration numbers, and the corresponding contributions from observation term (J_o) and constraint term (J_c).

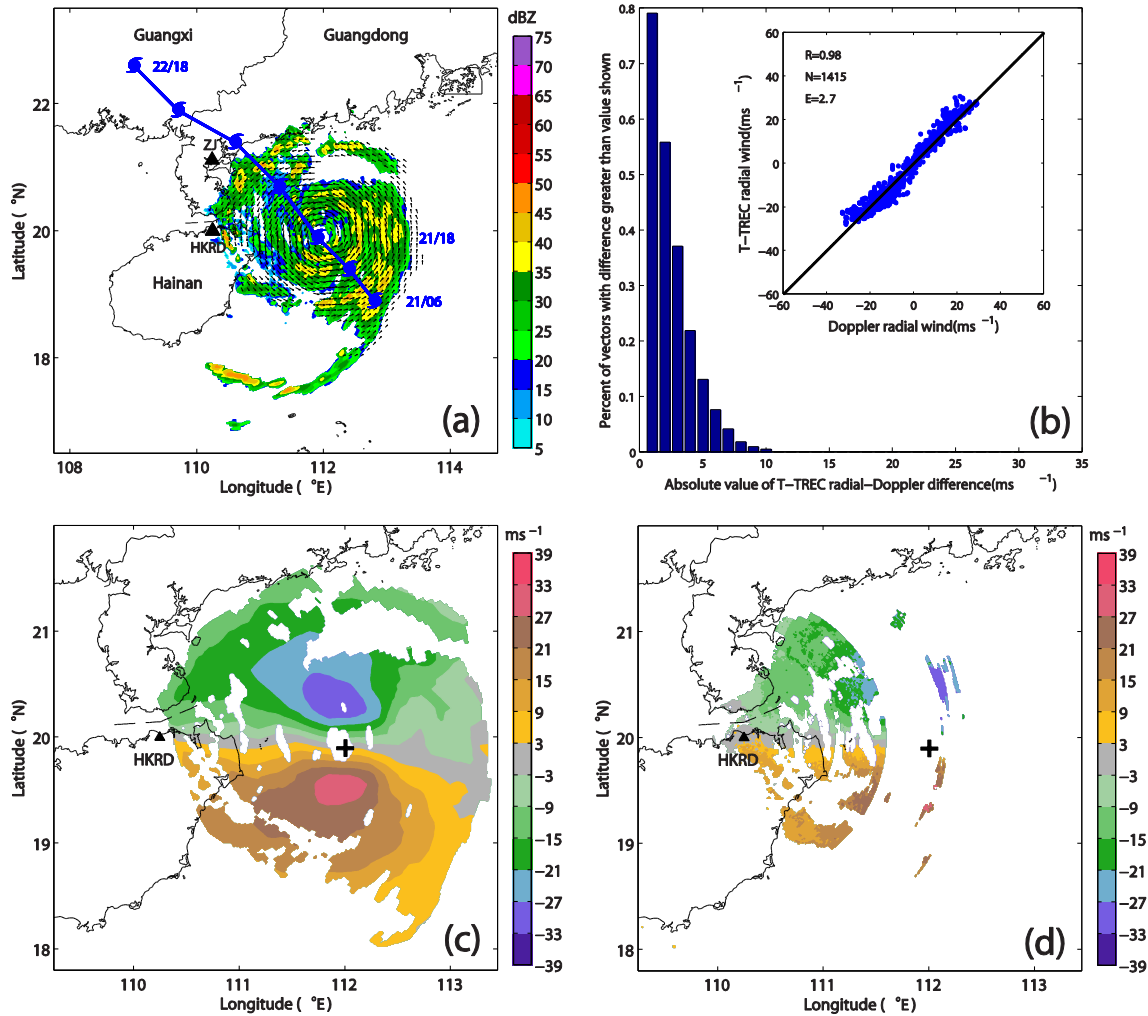


Fig. 3. The T-TREC-retrieved winds at 3-km height at 1800 UTC, 21 July. (a) T-TREC-retrieved wind vectors overlaid with the reflectivity (shaded, dBZ) and the JTWC best track locations of Typhoon Chanthu (2010) marked with 6-h interval from 0600 UTC, 21 July to 1800 UTC, 22 July, 2010; (b) Percent cumulative histogram of the difference between measured Doppler radial velocity and the retrieved radial component of T-TREC winds. N represents the total number of available radial velocities. R and E represent the correlation coefficient and the mean difference, respectively; (c) retrieved radial component of T-TREC-retrieved winds; and (d) the measured radial velocity from HKRD. '+' in (c) and (d) denote the center of typhoon.

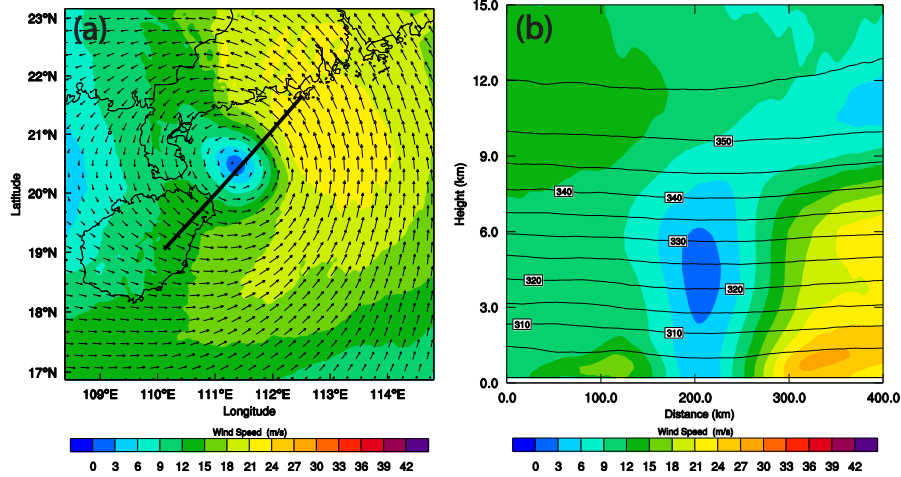


Fig. 4. The background field at 1800 UTC, 21 July, for DA experiments: (a) the horizontal wind vectors and speed (color shaded, m s^{-1}) at 3-km height; (b) southwest-northeast vertical sections of potential temperature (solid contours) and horizontal wind speed (color shaded, m s^{-1}). The thick solid line in (a) indicates the vertical cross section for (b).

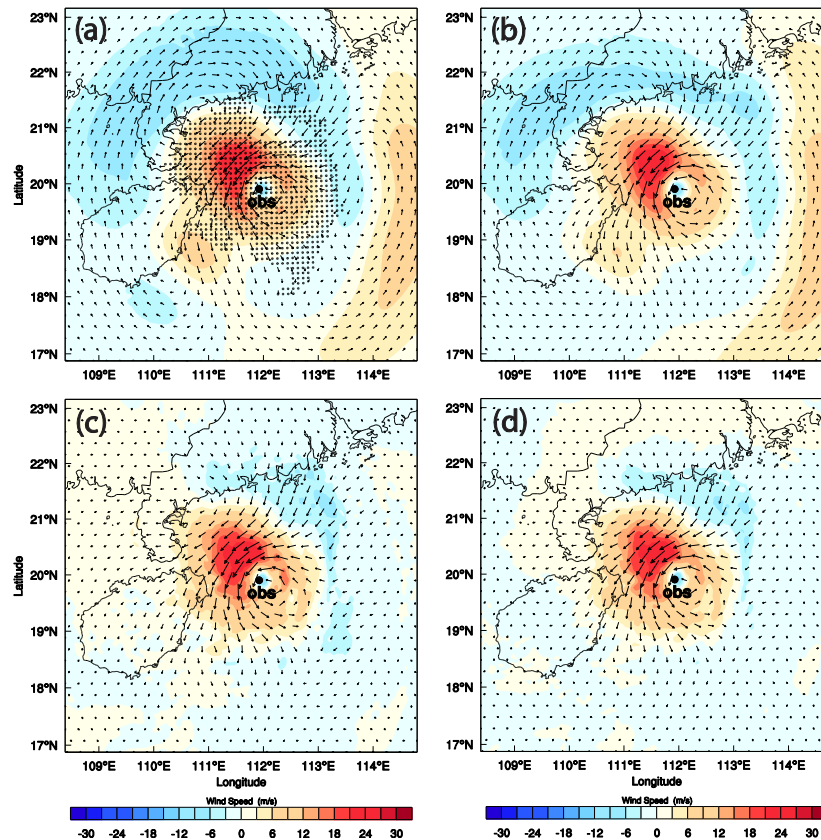


Fig. 5. Analysis increments of horizontal wind vectors (vectors) and wind speed (shaded, m s^{-1}) at 3-km height for (a) 3DVAR, (b) 3DVAR-DC, (c) En3DVAR, and (d) En3DVAR-DC at 1800 UTC, 21 July. The small circles in (a) represent the observation locations for T-TREC-retrieved winds. The black dot labeled “obs” indicates the JTWC best-track TC center position at this time.

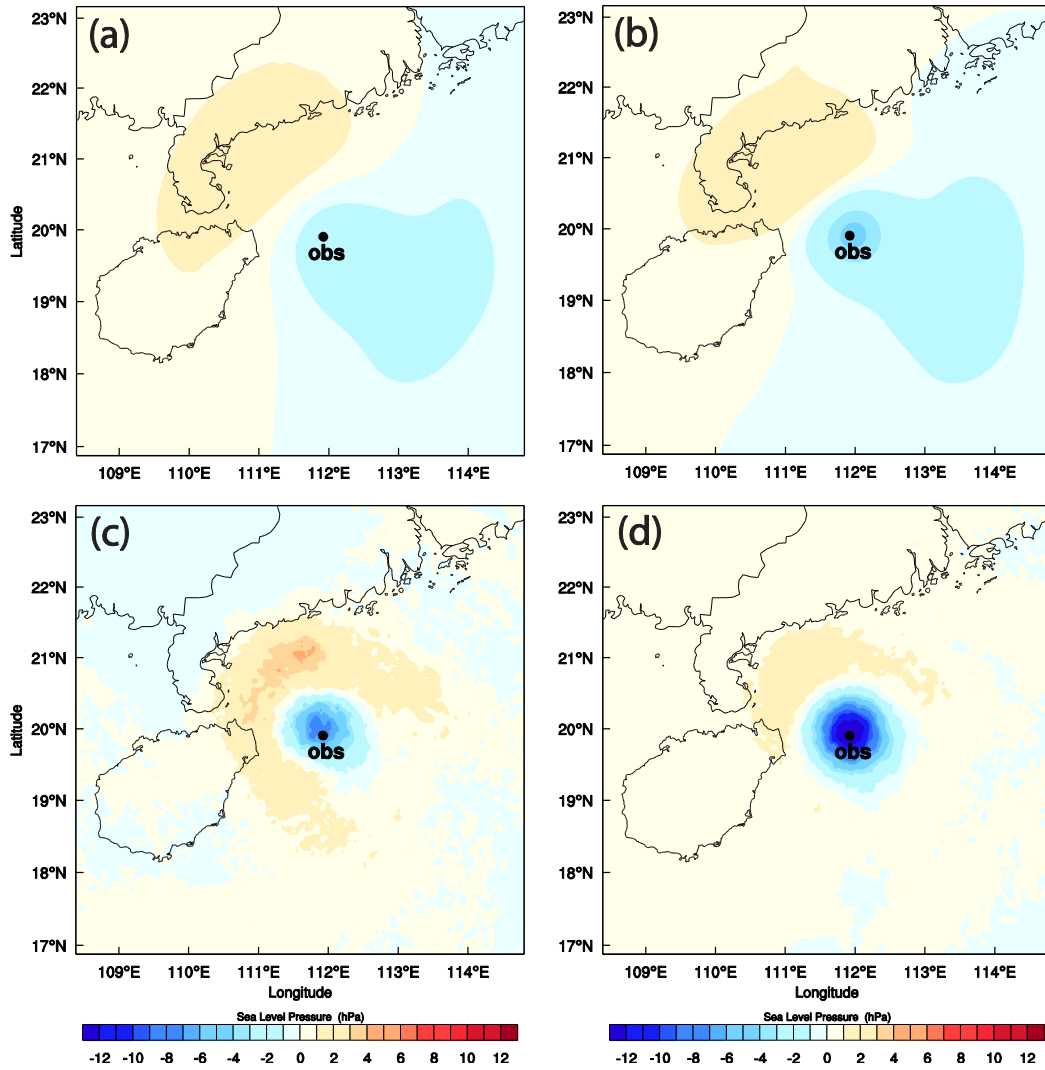


Fig. 6. Analysis increments of sea level pressure (shaded, hPa) for (a) 3DVAR, (b) 3DVAR-DC, (c) En3DVAR, and (d) En3DVAR-DC at 1800 UTC, 21 July. Black dot and “obs” are for JTWC best-track position of TC center at this time.

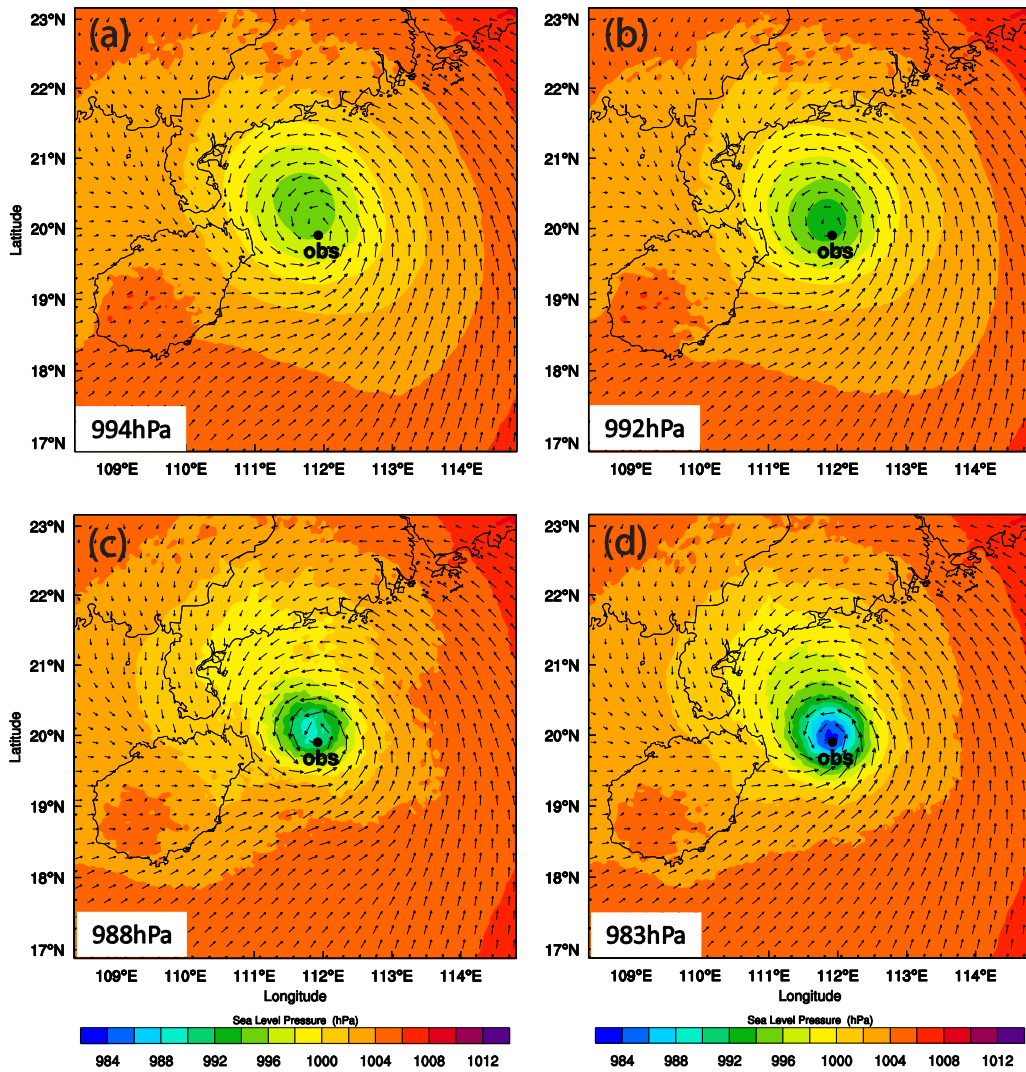


Fig. 7. The analyzed sea level pressure (shaded, hPa) and the surface wind vectors for (a) 3DVAR, (b) 3DVAR-DC, (c) En3DVAR, and (d) En3DVAR-DC at 1800 UTC, 21 July. Minimum SLP is shown at the lower corner of each figure. Black dot and “obs” are for JTWC best-track position of TC center at this time.

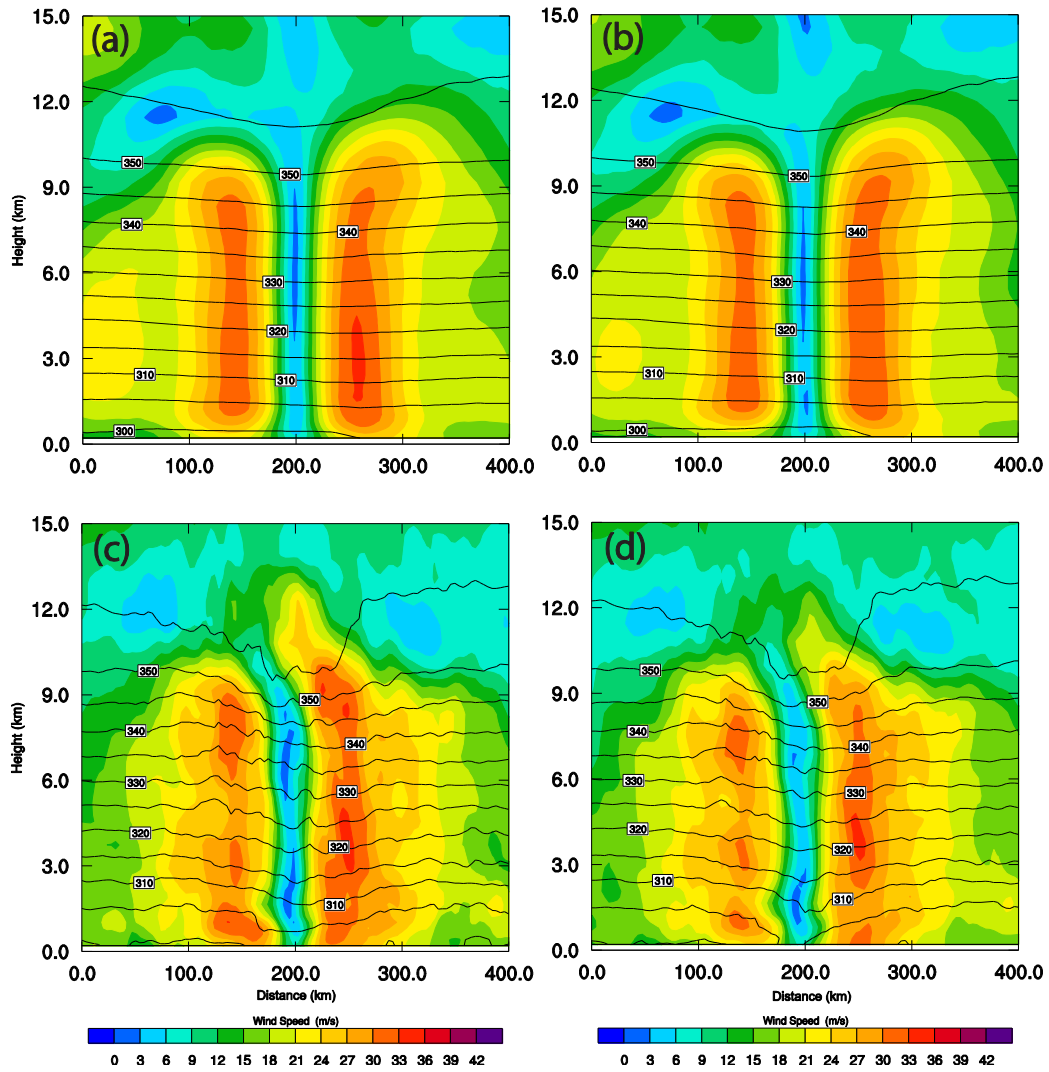


Fig. 8. Southwest-northeast vertical cross sections of analyzed horizontal wind speed (shaded, m s^{-1}) and potential temperature (solid contours, K, intervals: 5 K) through the TC center for (a) 3DVAR, (b) 3DVAR-DC, (c) En3DVAR, and (d) En3DVAR-DC at 1800 UTC, 21 July.

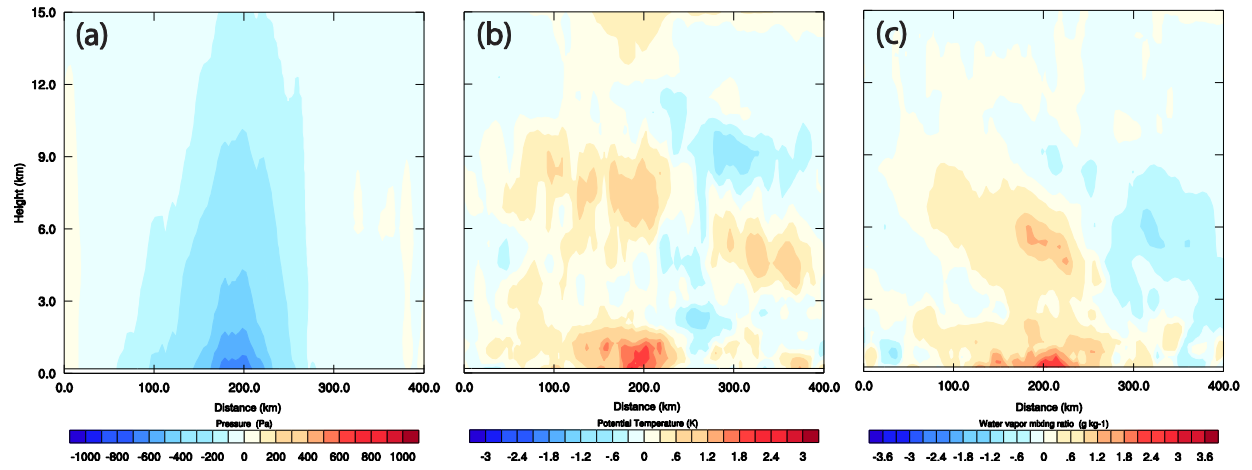


Fig. 9. The differences of analyzed fields between En3DVAR-DC and En3DVAR in the southwest-northeast vertical cross section through the TC center: (a) pressure (hPa), (b) potential temperature (K) and (c) water vapor mixing ratio (g kg^{-1}).

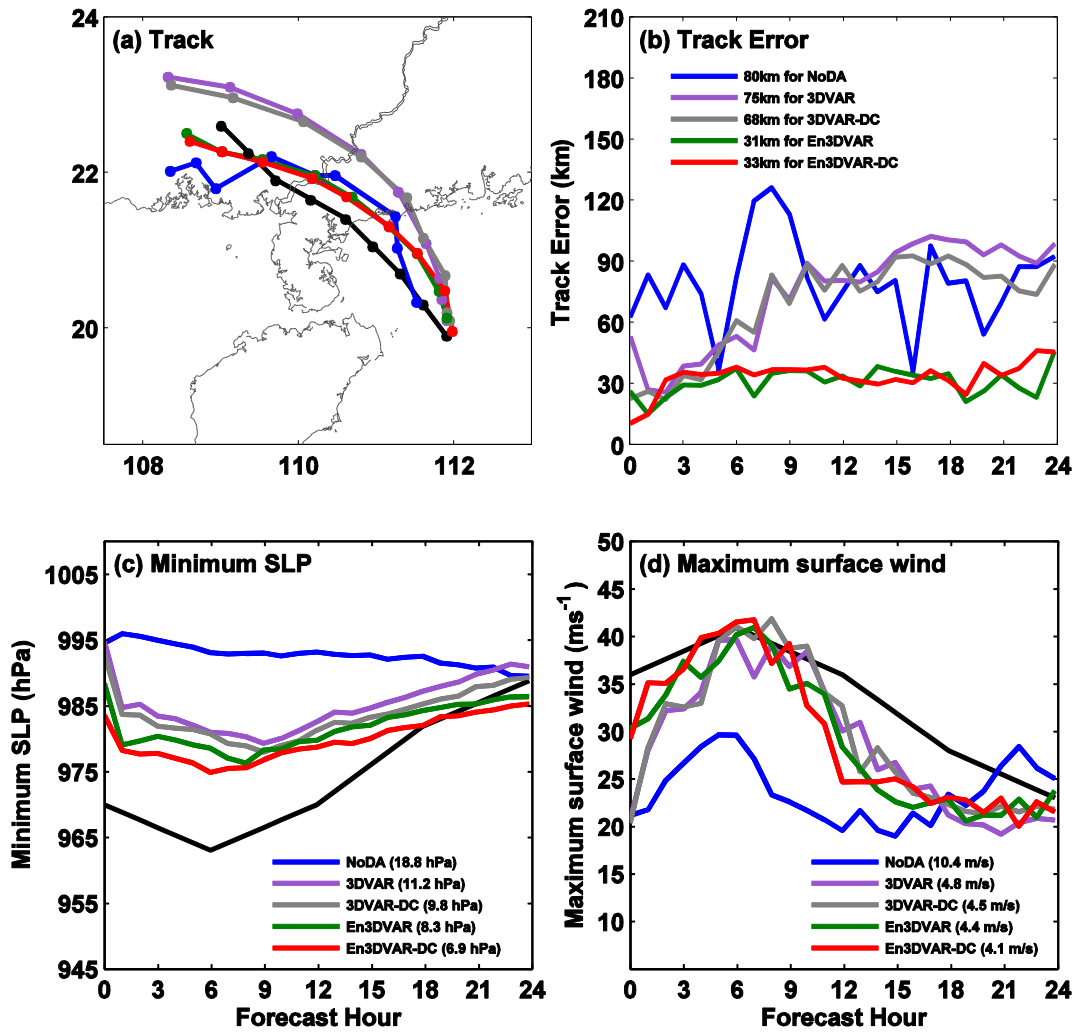


Fig. 10. The 24-h predicted (a) tracks, (b) track errors (km), (c) MSLP (hPa), and (d) MSW (m s^{-1}), for typhoon Chanthu (2010), from 1800 UTC, 21 July to 1800 UTC, 22 July 2010. The numbers in (b), (c) and (d) represent the mean track errors, MSLP errors and MSW errors, respectively, over the 24 hours period. JTWC best track data are shown in black in (a, c, d) and the dots on the plotted tracks in (a) are 3 hours apart.

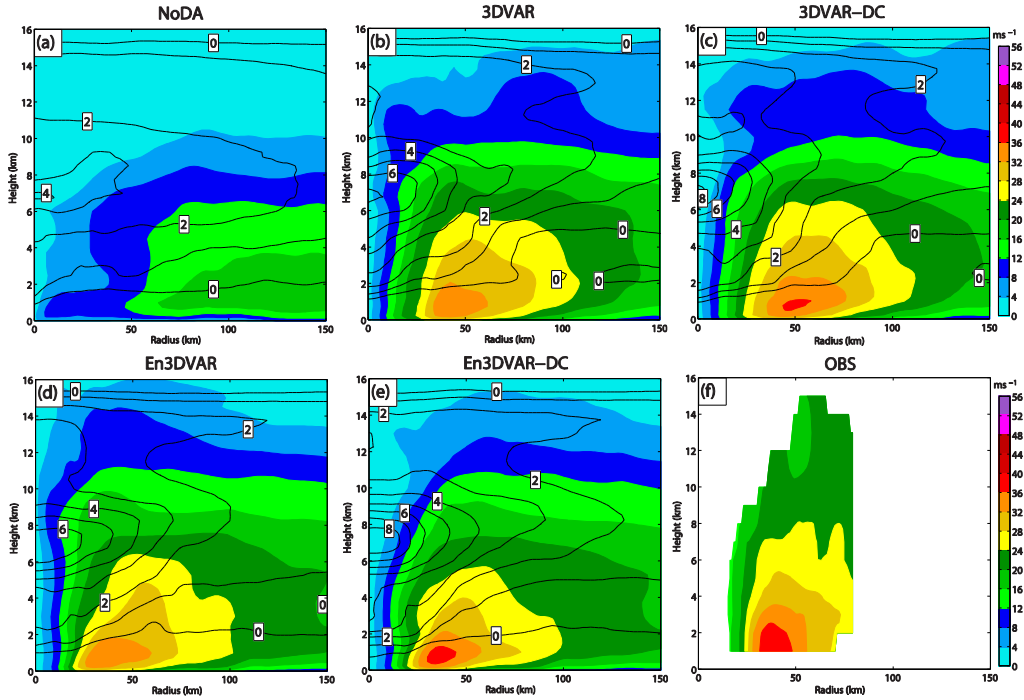


Fig. 11. Azimuthal mean tangential wind speed (shaded, m s^{-1}) and temperature deviation from horizontal mean (solid contours, K) of the 9-hour forecast valid at 0300 UTC, 22 July, for experiments (a) NoDA, (b) 3DVAR, (c) 3DVAR-DC, (d) En3DVAR, and (e) En3DVAR-DC, as compared with the (f) GBVTD-derived azimuthal mean tangential wind.

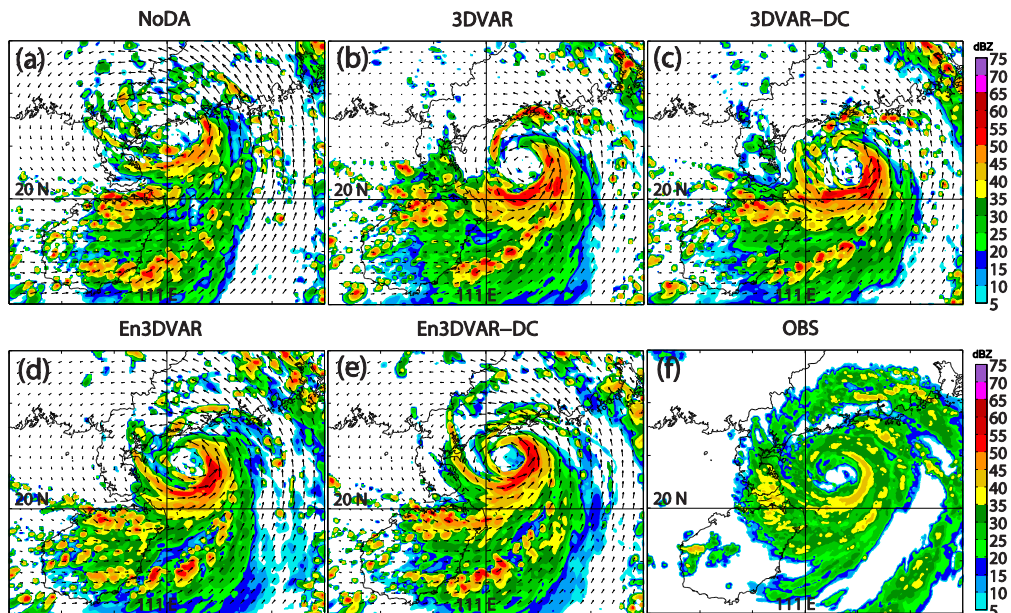


Fig. 12. Composite reflectivity (color shaded) and wind vectors at 3-km height predicted by experiments (a) NoDA, (b) 3DVAR, (c) 3DVAR-DC, (d) En3DVAR, and (e) En3DVAR-DC as compared to (f) observed composite reflectivity, at 0000 UTC, 22 July.

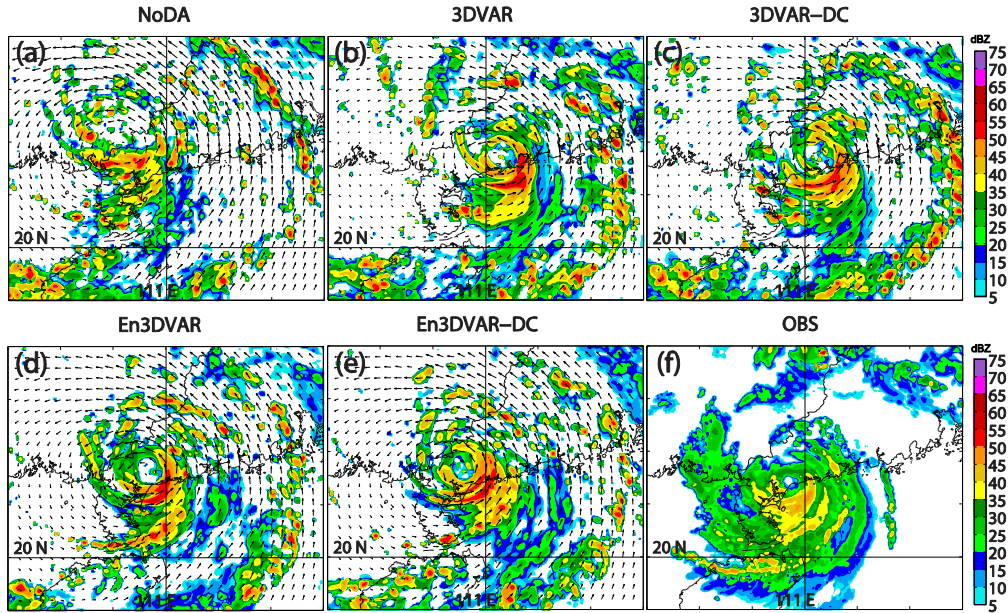


Fig. 13. Same as Fig. 12, but for the time of 0600 UTC, 22 July.

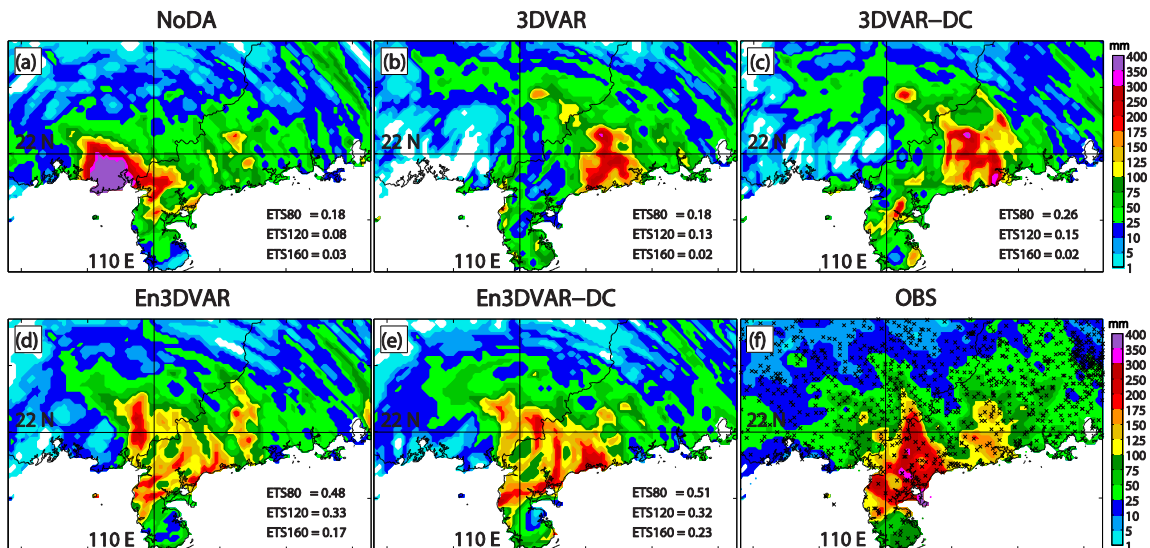


Fig. 14. 24-h accumulated precipitation (mm) valid at 1800 UTC, 22 July and the corresponding Equitable threat scores for the thresholds of 80 mm, 120 mm and 160 mm, respectively, from (a) NoDA, (b) 3DVAR, (c) 3DVAR-DC, (d) En3DVAR, (e) En3DVAR-DC, along with (f) automatic weather station observations. Symbols “x” in (f) indicate the locations for automatic weather stations.

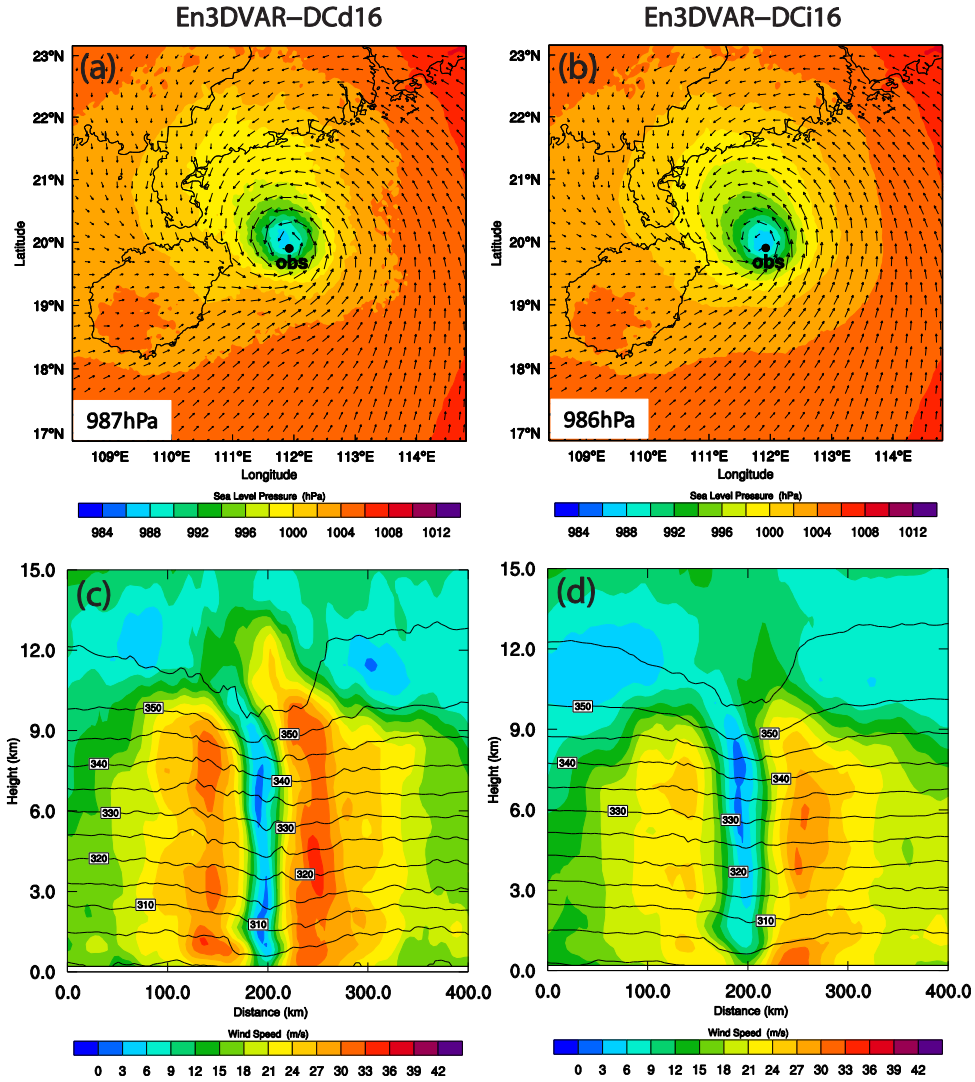


Fig. 15. The analyzed sea level pressure (shaded, hPa) and the surface wind vectors for (a) En3DVAR-DCd16 and (b) En3DVAR-DCi16 with the Minimum SLP shown at the lower corner of each figure, and the southwest-northeast vertical cross sections of analyzed horizontal wind speed (shaded, m s^{-1}) and potential temperature (solid contour, K, intervals: 5 K) for (c) En3DVAR-DCd16 and (d) En3DVAR-DCi16, at 1800 UTC, 21 July.

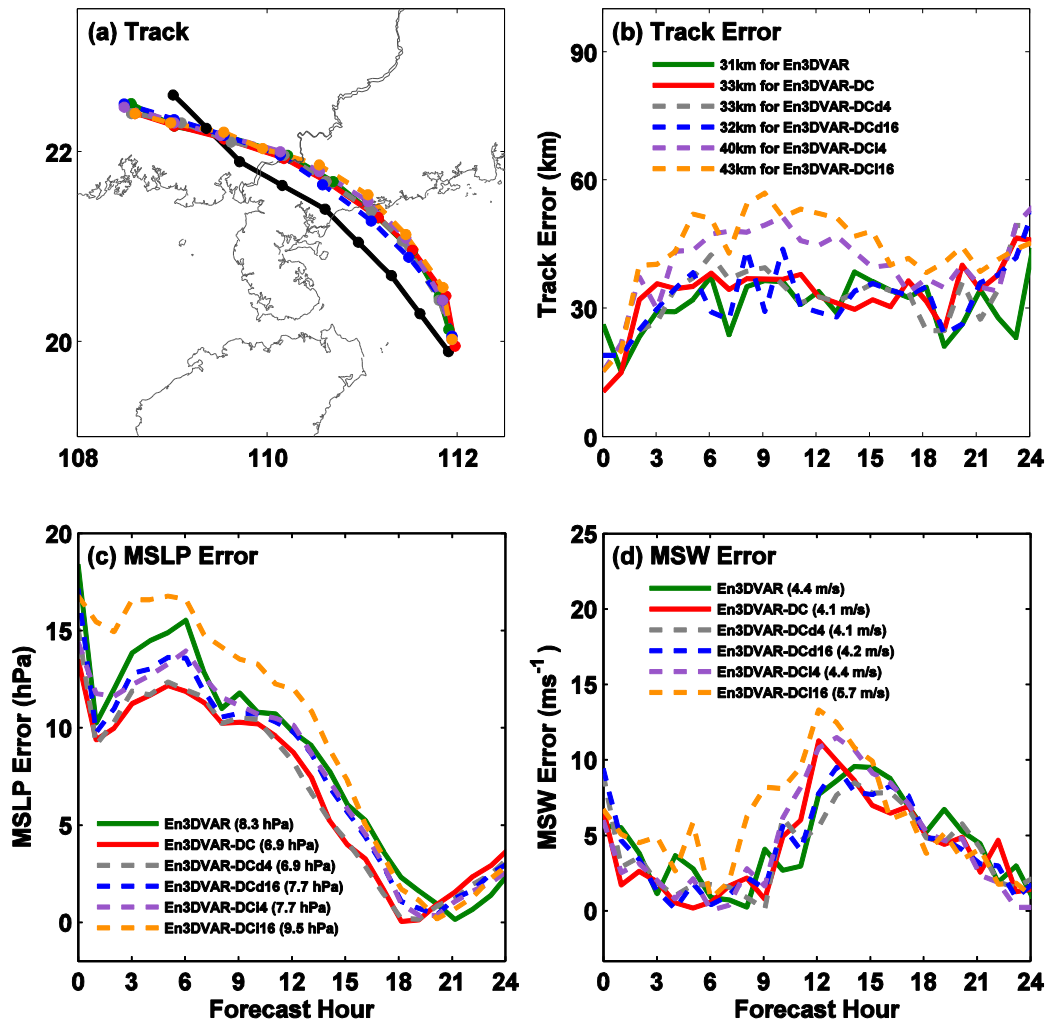


Fig. 16. The 24-h predicted (a) tracks, (b) track errors (km), (c) MSLP errors (hPa), and (d) MSW errors (m s^{-1}), for experiments En3DVAR-DCd4, En3DVAR-DCd16, En3DVAR-DCi4, En3DVAR-DCi16, along with En3DVAR and En3DVAR-DC, from 1800 UTC, 21 July to 1800 UTC, 22 July 2010. The numbers in (b), (c) and (d) represent the mean track errors, MSLP errors and MSW errors, respectively, over the 24 hours period. JTWC best track data are shown in black and 3 hours apart in (a).